Review

Methods for Physical Characterization of Phase-Separated Bodies and Membrane-less Organelles

Diana M. Mitrea[1], Bappaditya Chandra[1,†], Mylene C. Ferrolino[1,†], Eric B. Gibbs[1,†], Michele Tolbert[1,†], Michael R. White[1,†] and Richard W. Kriwacki[1,2]

*1 - **Department of Structural Biology,** St. Jude Children's Research Hospital, Memphis, TN 38105, USA*
*2 - **Department of Microbiology,** Immunology and Biochemistry, University of Tennessee Health Sciences Center, Memphis, TN 38163, USA*

***Correspondence to Diana M. Mitrea and Richard W. Kriwacki:** R.W. Kriwacki is to be contacted at: Department of Structural Biology, St. Jude Children's Research Hospital, Memphis, TN 38105, USA. diana.mitrea@stjude.org; richard.kriwacki@stjude.org*
https://doi.org/10.1016/j.jmb.2018.07.006
Edited by Julie Deborah Forman-Kay

Abstract

Membrane-less organelles are cellular structures which arise through the phenomenon of phase separation. This process enables compartmentalization of specific sets of macromolecules (e.g., proteins, nucleic acids), thereby regulating cellular processes by increasing local concentration, and modulating the structure and dynamics of their constituents. Understanding the connection between structure, material properties and function of membrane-less organelles requires inter-disciplinary approaches, which address length and timescales that span several orders of magnitude (*e.g.*, Ångstroms to micrometer, picoseconds to hours). In this review, we discuss the wide variety of methods that have been applied to characterize the morphology, rheology, structure and dynamics of membrane-less organelles and their components, *in vitro* and in live cells.

Introduction

Biochemical processes within eukaryotic cells are partially controlled through spatial and temporal organization of macromolecules. Cellular compartmentalization has long been appreciated, starting with early microscopic observations of unicellular organisms, and animal and plant tissues in the late 1600s, and later refined in the early 1950s through the advent of electron microscopy (EM) and improved sample preparation methods [1]. Two classes of subcellular compartments organize biological macromolecules within an eukaryotic cell. Membrane-bound organelles contain their components within a lipid bilayer membrane. Another type of compartments termed membrane-less organelles, however, is not delimited by membranes, but still maintains well-defined composition, structure, and function. For example, the nucleus, a membrane-bound organelle, contains a sub-compartment termed the nucleolus that lacks a surrounding membrane. Since the discovery of the nucleolus—the largest membrane-less organelle—in 1896 [2], advances in electron and fluorescence microscopy and the development of imaging methods that exceed the visible light diffraction limit on spatial resolution revealed that cells contain numerous other membrane-less organelles within the cytoplasm and the nucleus. However, an understanding of the physical basis for the formation of these cellular sub-compartments was elusive.

A breakthrough came through pioneering work by Brangwynne *et al.* demonstrating that membrane-less organelles such as P-granules [3] and nucleoli [4] behave as dense, phase-separated liquids in live cells. Spurred by these observations, studies from many laboratories have addressed: (1) mechanisms underlying the formation of membrane-less organelles, (2) their composition and physicochemical properties, and (3) the relationships between their dense-phase structure and the functions performed within them. Phase-separated bodies can arise from demixing of a single component, or a mixture of two or more components, termed homotypic and heterotypic phase separation, respectively (see

Box 1), to form dynamic, interconnected molecular networks. In homotypic phase-separated bodies, the intermolecular networks are formed *via* self-interaction of the single component. In heterotypic phase-separated bodies, multiple types of pairwise interactions (e.g., component A–component A, component A–component B, etc.) can contribute to the formation of intermolecular networks. The molecular organization within these organelles spans a broad range of length scales, ranging from intra- and intermolecular contacts [on the Ångstrom (Å) length scale] to extended inter-molecular networks [on the nanometer (nm) to micrometer (μm) length scale]. Furthermore, a wide range of timescales must be considered when addressing the molecular dynamics within membrane-less organelles, including the timescale of conformational fluctuations [on the picosecond (ps) to nanosecond (ns) timescale] and association/dissociation events [on the microsecond (μs) to millisecond (ms) timescale] in addition to slow network rearrangements (on the hour to day timescale). Consequently, multiple, complementary approaches must be integrated to address questions related to the structure, dynamics, and biology of membrane-less organelles. For example, theories that originated in the field of polymer physics [5–8] are commonly used to model phase separation by proteins [9, 10] and to develop computational models that describe the process of demixing [11–14]. NMR spectroscopy is used to probe the conformational and dynamic features of proteins within phase-separated droplets *in vitro* with atomic resolution [10, 15, 16]. The bulk properties of phase-separated structures, both *in vitro* and within cells, as well as the diffusive properties of individual macromolecules within them, are probed using fluorescence microscopy. Here, we review the methods employed in studies of membrane-less organelles in cells and *in vitro* phase-separated bodies across diverse length and timescales, noting their specific applications, the information provided, and the associated advantages and disadvantages. We review, (1) imaging methods that probe molecular dynamics, structural organization on the nm to μm length scales, and the viscoelastic properties of phase-separated bodies; (2) methods used for the characterization of thermodynamic, kinetic, and structural properties of proteins within them and their interactions on the Å to nm length scale; and (3) computational methods that probe length and timescale gaps that are currently beyond the reach of experimental approaches (Fig. 1).[‡]

Box 1
Glossary.

Demixing
Phenomenon by which, in order to minimize the solvation energy, one or more polymers (e.g., proteins, nucleic acids, etc.) desolvate from a homogeneous solution to form two coexisting, yet immiscible, phases termed the dense and light phases (synonymous with phase separation). The dense phase is characterized by increased local concentration and viscosity, while the light phase is depleted of polymer(s).

Low-complexity regions
Protein regions characterized by amino acid bias and/or by repetitive linear motifs; this amino acid composition is often associated with structural disorder.

Homotypic interactions
Phase separation-driving interactions which occur between polymers of the same type (i.e., self-interaction)

Heterotypic interactions
Phase separation-driving interactions which occur between polymers of different types

Binodal curve
The curve within the phase diagram that defines the boundary conditions where the energies of the system in the mixed and demixed state are equivalent

Spinodal curve
The curve within the phase diagram that defines the boundary conditions where the demixed state of the system is energetically favorable with respect to the mixed state

Morphological Characterization of Membrane-less Organelles

While the ability of various membrane-less organelles to undergo fusion and dynamic exchange of components with the surrounding milllieu was previously appreciated [17–22], the liquid-like nature of membrane-less organelles in live cells was first demonstrated using time-lapse light microscopy imaging showing that P-granules flow over obstacles, such as the nucleus [3], and undergo fission and fusion [3, 4]. With several modalities available, including differential interference contrast (DIC) [23–26] and fluorescence-detection [15, 23, 25, 27, 28], light microscopy is routinely used to visualize macromolecular phase separation *in vitro* and in live cells, as discussed in the following section.

Light microscopy

Light microscopy techniques proffer spatial resolution ranging from ~200 nm to 1 mm, with the lower

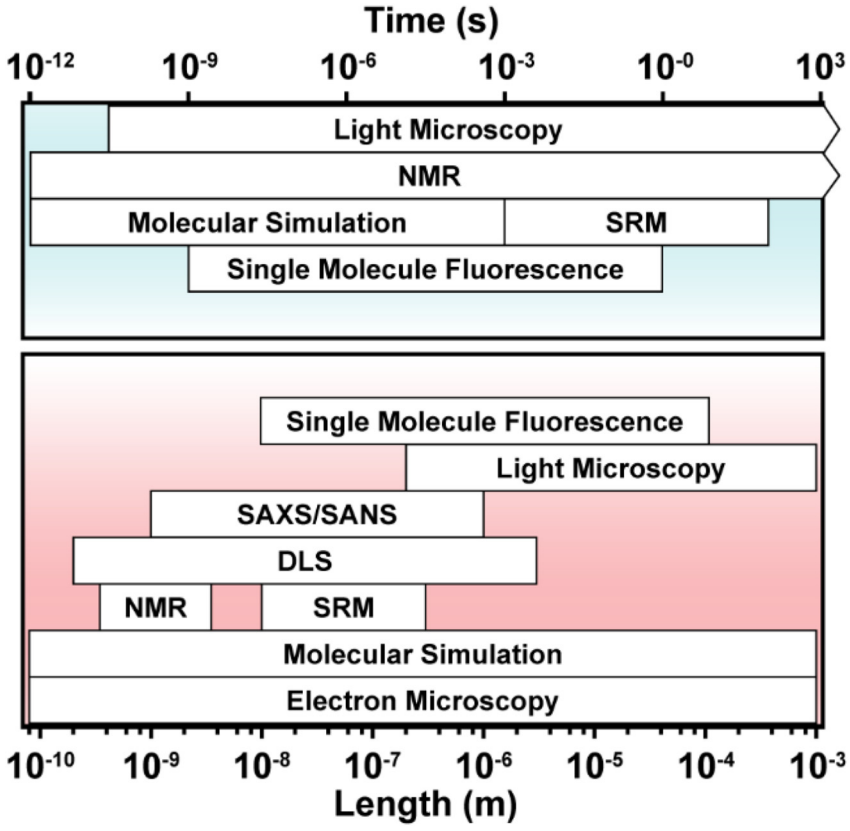

Fig. 1. Biophysical methods used in characterization of membrane-less organelles. The relevant time (top, blue region) and length (bottom, red region) scales are shown for each of the techniques discussed in this review (SRM, super-resolution microscopy). By combining several methodologies, the structural and dynamic features of membrane-less organelles, and the molecules within them, can be characterized on the timescale between picoseconds and hours, and on the length scale between Ångstroms and millimeters.

limit determined by diffraction [29]. Time resolution spans ms to days, with the lower limit determined by the speed of lasers, detectors, and computer-controlled electronics [29]. Light microscopy is suitable for visualization of membrane-less bodies in live and fixed cells, as well as *in vitro* [4, 23, 24, 26, 30–37]. Sample fixation stabilizes intermolecular interactions and preserves cellular architecture, and allows visualization of endogenous proteins *via* immunofluorescence [38]. Because molecular dynamics are disrupted in the process of sample fixation, and immunolabeling can affect epitope accessibility, and consequently alter the distribution of the immune-targeted component within cells [38], this method of sample preparation has limited applications in the study of membrane-less organelles. The use of live cells expressing fluorescent fusion proteins is better suited for real-time visualization of molecular dynamics inside cells. However, live cell imaging requires maintenance of optimal cell culture conditions and minimal phototoxicity during image acquisition [38]. In addition, heterologous protein expression often does not reflect the endogenous cellular levels, resulting in alteration of the properties of the membrane-less organelles under study.

Contrast-based imaging methods, such as phase contrast and DIC, are advantageous because microscopic structures can be observed without introduction of extrinsic fluorophores. These imaging methods rely on intrinsic differences in the refractive index or thickness of structures within a sample, which alters the phase of the diffracted light. Phase differences in the diffracted light are converted into intensity differences as a function of the specimen's optical path length, thus yielding a dark image for dense regions of the specimen against a light background [39]. DIC uses optical path length gradients to generate contrast in the specimen and yields images that appear three-dimensional [39].

Phase contrast and DIC are well suited for visualizing dense internal cellular structures; however, DIC is better suited to resolve cell boundaries [40]. DIC imaging has been used to determine the saturation concentrations, where formation of *in vitro* protein droplets occurs, such as those comprising the RGG domain of Ddx4 [23], LAF-1 [25], tau [26], and HP1α [36], and also for imaging dense membrane-less organelles in live cells, including Cajal bodies [41] and nucleoli [4]. Time-lapse DIC imaging was also employed to demonstrate the liquid-like properties of nucleoli by monitoring their fission and fusion [4]. While contrast-based imaging methods provide information on the overall morphology of dense cellular bodies, including membrane-less organelles, selective tracking of specific components of interest is not

possible. Fluorescence-detected microscopy is used for these applications.

Fluorescence microscopy detects fluorophores that are genetically [42, 43], chemically [44], immunologically [45] or enzymatically [46, 47] linked to a macromolecule of interest. The entire specimen is excited with a laser tuned to the excitation wavelength of the fluorophore and the resulting emitted light is detected. A wide range of fluorescent probes (fluorescent proteins and dyes) are commercially available, making fluorescence microscopy a versatile technique for analysis of both live and fixed specimens. In addition, fluorescent dyes that exhibit binding specificity for certain classes of macromolecules or structural features (e.g., DNA/RNA intercalators [48], amyloidophilic dyes, etc.) are used in fluorescence microscopy applications to monitor their localization and conformational changes, both in live cells and *in vitro.* For example, thioflavin-T, a fluorescent dye with binding specificity for β-sheet structural features characteristic of amyloid fibrils [49], classically used to study amyloid fibers, was used to visualize time-dependent conformational changes associated with aging and morphological changes within hnRNP A1 liquid-like droplets *in vitro* [24]. However, the mechanism underlying the binding of thioflavin-T to amyloid fibers is not fully understood and the efficiency of its binding to various types of amyloid fibers is variable. For example, amyloids formed with FUS exhibit low thioflavin-T affinity [50]. Caution should be exercised, and appropriate corrections applied, when quantitatively interpreting fluorescence intensity data obtained from thioflavin-T in phase-separated bodies, as its quantum yield increases with viscosity [51]. The influence of the fluorescent probe (i.e., a protein or chemical dye) attached to the protein or nucleic acid of interest on the phase behavior should be carefully investigated, as their presence may introduce additional binding valency (i.e., GFP dimerization, fluorescent dye π–π stacking) or interfere with binding between labeled macromolecules.

Fluorescently labeled macromolecules are most commonly detected using wide-field or confocal fluorescence microscopy (reviewed in ref. [52]). In wide-field fluorescence microscopy, fluorophores are uniformly illuminated and excited over the entire field of view. This provides high contrast and sensitivity with short acquisition times for two-dimensional imaging of thin specimens (<30 μm) [52]. For samples thicker than 30 μm, though, fluorescence originating outside of the focal plane reduces contrast, and causes image blurring and lower resolution [52].

Confocal fluorescence microscopy methods prevent this blurring by blocking light originating from out-of-focus planes using a spatial pinhole [52]. This method improves contrast at the expense of the signal-to-noise ratio and acquisition times, which decrease and lengthen, respectively, as compared to wide-field imaging. However, signal reduction can be compensated by increasing the intensity of the excitation laser; also, several current confocal microscopy modalities offer improved image acquisition speeds [52]. Due to its high-resolution and sensitivity, confocal fluorescence microscopy is routinely used to analyze the localization of fluorescently labeled macromolecules within membrane-less organelles and to monitor morphological changes within them (e.g., within those that are >200 nm in diameter, such as nucleoli). It is also widely used to study phase-separated droplets prepared *in vitro* (Fig. 2 and c). Specialized spectral imaging techniques can be used to simultaneously monitor the localization of multiple, differently labeled components within phase-separated bodies [53].

The photons detected in confocal fluorescence microscopy originate within a horizontal plane at a specific *Z*-axis position, which allows 3D image reconstruction from multiple 2D images acquired at different *Z*-axis positions [44]. Time-resolved 3D image reconstruction, referred to as 4D fluorescence imaging, was used to monitor the movement of Cajal bodies within the nucleoplasm, their fission and fusion, and association with nucleoli [33].

The quantitative analysis of confocal images provides information on labeled components, including dynamics, concentration, and co-localization of multiple, differently labeled biomolecules. However, understanding the sources of potential artifacts and the inclusion of appropriate controls is required to extract spatially accurate data from fluorescence microscopic images. For example, photo-damage to the specimen and photobleaching of fluorescent probes caused by laser illumination should be minimized and/or accounted for in image analysis, as discussed below.

Quantitative image analysis

Quantitative, steady-state image analysis

The integrated emitted light intensity of the excited fluorophore can be directly correlated with the amount of the fluorescently labeled macromolecule within a microscopically imaged region of interest (ROI). A calibration curve describing the linear relationship between the mean intensity per pixel obtained from image analysis of a series of fluorophore solutions of known concentrations is used to determine the concentration of the same fluorophore within the ROI in the sample. This analysis was used to quantify the nucleoplasmic concentration of GFP-labeled fibrillarin (FIB1) in *Caenorhabditis elegans* embryos [54], as well as the composition of heterotypic liquid-like droplets (prepared *in vitro* with polySUMO, polySIM, PTB, and RNA) as a function of the binding valency of the individual components [55]. It should be noted that a direct correlation between the

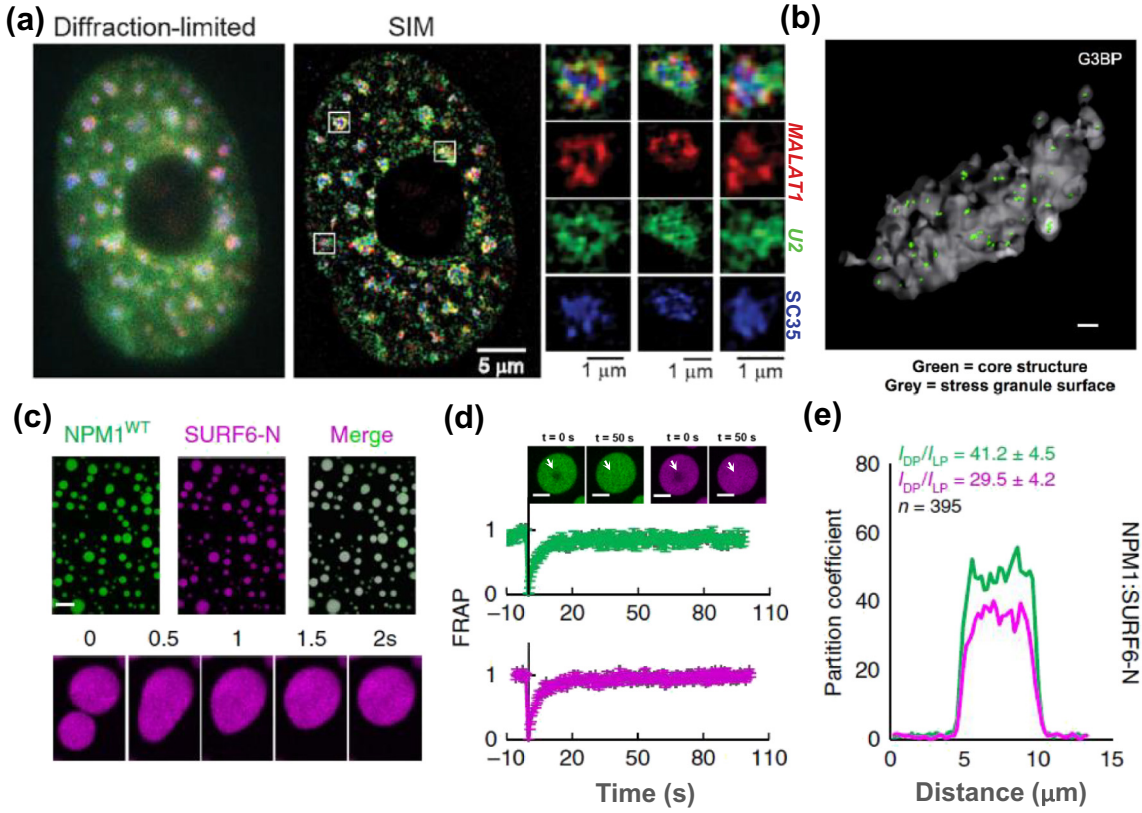

Fig. 2. Fluorescence and super-resolution microscopy in the study of phase-separated bodies, in cells and *in vitro.* (a) Sub-compartmentalization of nuclear speckles in WI-38 human cells nuclei, as visualized by wide-field fluorescence microscopy (left) and SIM (center). Intra-organelle demixing of *MALAT1* lncRNA (red), *U2* small nuclear RNA (green), and SC35 protein (blue) within one nuclear speckle is shown in the right panel. The figure was reproduced with permission from Fei *et al.* [11]. (b) 3D reconstruction obtained from STORM super-resolution imaging of the core–shell architecture of stress granules. The figure was reproduced with permission from Jain *et al.* [32]. (c) Confocal fluorescence microscopy images of *in vitro* heterotypic liquid-like droplets, formed with NPM1 and SURF6-N (top) and time-lapse snapshots of two fusing droplets (bottom). (d) FRAP recovery curves within an ROI at the center of the droplet, indicated by arrows, show near-complete recovery of NPM1 (top) and SURF6-N (bottom). (e) Fluorescence intensity profiles for NPM1 (green) and SURF6-N (magenta) through a linear cross-section through an imaged droplet. The partition coefficients were obtained from quantitative image analysis of the fluorescence intensity within droplets with respect to that within the light phase. Panels c–e were reproduced and modified from Mitrea *et al.* [27].

concentration of a fluorescent component and its intensity detected by fluorescence imaging is accurate when the size of the object quantified exceeds the dimension of the microscope's point spread function. Appropriate corrections, discussed in detail in ref. [56], are required in order to deconvolute the signal diluting effect of the point spread function on the absolute intensity, when analyzing smaller objects.

Specific macromolecular components are concentrated within membrane-less organelles through demixing from the surrounding milieu. The index of dispersion within a microscopic image, quantified as the variance in fluorescence intensity (σ^2) normalized per mean fluorescence intensity in the light phase (μ), was used as a measure of phase separation by Jain *et al.* [57]. The extent to which macromolecules are concentrated by phase separation is given by the partition coefficient, which quantifies the relative concentration of a specific component within the more concentrated dense phase (droplet) *versus* the surrounding, less concentrated light phase. The partition coefficient can be calculated from the ratio of concentrations, determined as described above [55], or of the fluorescence intensity measured in the dense and the light phases (Fig. 2c and e) [27, 55]. Importantly, the spectral properties, including the quantum yield of the fluorescent probes, are influenced by environmental factors, such as solvent polarity and viscosity [58]. Because the dense phase of phase-separated bodies is characterized by a marked increase in viscosity with respect to the surrounding environment, variations in the fluorophore quantum yield need to be considered in the calculation of concentrations and partition coefficients [27, 59]. While the optical properties of fluorescent proteins, such as EGFP and DsRed, are

essentially invariant in dilute aqueous solutions and inside live cells [60], the sensitivity of several types of chemical fluorophores to the physical properties of their microenvironments can be used to monitor physicochemical properties within phase-separated bodies *in vitro* and in live cells. For example, the ratiometric pH indicator fluorescent dye, SNARF-4F, was utilized to demonstrate that the local pH within nucleoli is lower than that of the surrounding nucleoplasm [61]. Viscosity-sensitive fluorophores or molecular rotors have also been used to characterize the viscoelastic properties of cellular membranes [62, 63].

In contrast to the steady-state imaging methods discussed above, time-resolved microscopy images can be quantitatively interpreted to extract information about macromolecular dynamics and the viscoelastic properties of phase-separated bodies. These methods are discussed in the following section.

Quantitative, time-resolved image analysis

As previously discussed, laser illumination of fluorescent reporters causes photobleaching, an effect that should be minimized in most imaging applications. This effect, however, can be leveraged to obtain quantitative information about the dynamics of fluorescently labeled components localized within phase-separated bodies. In fluorescence recovery after photobleaching (FRAP) and fluorescence loss in photobleaching (FLIP), the kinetics of fluorescence intensity re-equilibration after controlled photobleaching of the labeled molecules within an ROI are quantified. In both FRAP and FLIP, a specific ROI is illuminated with a high-intensity laser, at the excitation wavelength of the fluorophore, to irreversibly convert the molecules to a dark state [44]. The diffusion of unbleached and photobleached molecules into and out of the ROI, respectively, is then quantified by measuring the variation in fluorescence intensity as a function of time (Fig. 2d) [44]. We note, however, that fluorescence equilibration for highly mobile molecules can occur within several ms. Because the time resolution of the experiment depends on acquisition rate, the use of fast confocal microscopes (i.e., with the spinning disk configuration) is critical for detecting rapidly diffusing molecules.

FRAP assays monitor the diffusion of fluorescent molecules within the photobleached region and have been used to monitor diffusion of organic polymers, proteins, and lipids in the plasma membrane, cytoplasm, and nucleus [64, 65]. Diffusion can also inform on the viscoelastic properties of soft biomaterials, such as phase-separated bodies [64]. In particular, FRAP has been widely applied in studies of membrane-less organelles and *in vitro* phase-separated bodies (Fig. 2d). In its simplest form, FRAP can assess macromolecular mobility within membrane-less organelles and phase-separated bodies, an indicator of liquid-like behavior [9, 23, 24, 27, 66]. The rate of (or half-time for) fluorescence recovery of a photobleached component, as well as the extent of recovery, termed the mobile fraction, can be extracted from the evolution of the fluorescence intensity within a ROI, as described by Eq. (1) [44]:

$$I_t = M_f\left(1-e^{-kt}\right) \tag{1}$$

where I_t is the fluorescence intensity at time point t, M_f is the mobile fraction and k is the fitted recovery rate. The half-life ($\tau_{1/2}$) and mobile fraction of the diffusing species are given as:

$$\tau_{1/2} = \frac{\ln(0.5)}{-k} \tag{2}$$

$$M_f = \frac{I_\infty - I_0}{I_i - I_0} \tag{3}$$

where I_∞ represents the maximum, threshold intensity value after bleaching; I_0, the intensity immediately after bleaching; and I_i, the intensity before bleaching.

Equation (1) appropriately describes the fluorescence recovery of a homogenously diffusing species, as in the case of LAF-1 in phase-separated droplets [25]. Multi-exponential equations (not shown) must be employed if the diffusing macromolecule is present as two or more species within the ROI, as was shown for hnRNP A1 in liquid-like droplets [24]. A global fit model can also be employed, from which the half-time of recovery, averaged over all observable species, is obtained [67]:

$$I_t = \frac{I_0 + I_\infty \dfrac{t}{\tau_{1/2}}}{1 + \dfrac{t}{\tau_{1/2}}} \tag{4}$$

The diffusion coefficient (D) of the observed species can be estimated from the $\tau_{1/2}$ value (Eq. (5)) [25, 68]. Furthermore, the apparent hydrodynamic radius of the diffusing species can be obtained using the Stokes–Einstein equation (Eq. (6)):

$$D \approx r^2/\tau_{1/2} \tag{5}$$

$$D = \frac{k_B T}{6\pi\eta R_h} \tag{6}$$

where r is the effective radius of the ROI (see ref. [67]), k_B is the Boltzmann constant, T is the temperature (in Kelvin), η is the viscosity, and R_h is the hydrodynamic radius of the diffusing species. This type of analysis is appropriate for components in phase-separated

systems that exhibit uniform size and shape [10, 23, 25]. The accurate determination of the viscosity within phase-separated bodies is required for this analysis and methods for characterization of the viscoelastic properties of membrane-less organelles are discussed below. In the case of homotypic phase separation by Ddx4, the diffusion coefficient and an apparent R_h obtained from FRAP experiments [23] were in good agreement with values of these parameters determined by NMR [10]. The calculated apparent R_h value reflects the convolution of the true molecular size with the influence of quinary interactions between neighboring molecules [10]. We note that more advanced methods for the analysis of FRAP data to obtain information on molecular dynamics have been developed but are beyond the scope of the current review [69, 70].

FLIP is often used to complement FRAP. After photobleaching an ROI within the sample, the decrease in fluorescence of another ROI located in the same field of view as the first, that has not been photobleached, is monitored. In contrast to FRAP, FLIP quantifies the re-equilibration of photobleached and fluorescent molecules within an un-bleached ROI of the sample. A combination of FRAP and FLIP was used by Brangwynne *et al.* [3] to illustrate the dynamics of GFP-labeled PGL-1 within P granules *in vivo*. Photobleaching of half of one P granule was followed by fluorescence recovery on the seconds timescale in the treated area, concomitant with loss of fluorescence in the untreated area, indicating diffusion-limited re-equilibration of the fluorescently tagged molecules within this membrane-less organelle [3].

Several potential sources of artifacts must be considered in the quantitative interpretation of photobleaching results. High-intensity laser illumination can cause phototoxicity to live cells, potentially altering signaling pathways and, consequently, the properties and composition of membrane-less organelles that respond to stress. Similarly, high-intensity laser exposure can promote protein cross-linking, therefore interfering with protein activity, diffusion, and/or conformational dynamics. Cross-linking, in particular, can result in artifactually static behavior of the protein characterized by FRAP; therefore, this effect should be examined at the onset of the experiment and illumination conditions altered if observed. Most commonly, global photobleaching of samples can occur due to prolonged laser exposure during time-lapse image acquisition. This effect can be accounted for by applying appropriate correction factors determined by analyzing an ROI not exposed to high-intensity illumination (for a detailed protocol, see ref. [67]).

Many hypothesize that the biological functions that occur within membrane-less organelles are sensitive to changes in their morphology, viscoelastic properties, and internal dynamics, and methods such as FRAP and FLIP, and others, can be used to correlate these physical properties with function. For example, treatment of cells with actinomycin D, which blocks rRNA transcription in the dense fibrillar component (DFC) of the nucleolus due to inhibition of RNA Polymerase I, causes changes in the nucleolar proteome [71], which is associated with stiffening of nucleoli as measured using atomic force microscopy [72]. Furthermore, ATP depletion reduced translocation of the highly abundant phosphoprotein, Nucleophosmin (NPM1), into nucleoli [73] and, years later, was shown, through real-time fluorescence imaging measurements of nucleolar fusion and determination of inverse capillary velocity values (discussed below), to increase the viscosity of nucleoli 10-fold [4]. In addition, genetic deletion of the nucleolar protein, $p19^{Arf}$, which binds to NPM1 [74, 75], is associated with enlargement of nucleoli observed using fluorescence imaging and enhanced ribosome biogenesis [76]. Importantly, irreversible changes in the physical properties of membrane-less organelles are associated with disease. For example, fluorescence light microscopy showed that phase-separated bodies formed by hnRNP A1/2 [24, 77, 78], FUS [66, 79, 80], TDP-43 [81], and Tau [26, 82] transition from liquid-like behavior to fibrous aggregates. FRAP was used to show that changes in molecular dynamics were associated with the observed morphological changes. Clearly, fluorescence microscopy methods, and complementary techniques, will be essential for broadly establishing links between the physical properties of membrane-less organelles and the functions that occur within them, and how these links are altered in disease.

The size of many membrane-less organelles, such as RNP granules [32], is near the light diffraction limit and this precludes detailed morphological characterization using conventional light microscopy. The same limitations apply for larger organelles, such as the nucleolus (~0.5 to 9 μm in diameter [83]), which exhibits sub-structural organization on length scales below the diffraction limit. Thus, imaging methods that resolve length scales below the diffraction limit are required to fully understand the structural features of membrane-less organelles; some of these techniques are highlighted below.

Super-resolution microscopy

Super-resolution microscopy combines optical inputs with mathematical analysis to construct images of specimens with resolutions 2- to 10-fold below the diffraction limit (reviewed in ref. [84]); several methods are discussed below.

Structured illumination microscopy (SIM) is a wide-field fluorescence microscopy method that can achieve XY and axial resolutions of 100–130 and 300 nm, respectively, with a temporal resolution of ms to s. Improved resolution is achieved using interference-generated light patterns, due to the

Moiré effect. Post-acquisition image processing is used to extract information below the diffraction limit [84]. Because SIM uses the wide-field fluorescence microscopy optical configuration, live and fixed specimens can be labeled using conventional fluorescent probes, with up to four different colors visualized simultaneously [84]. Articles by Demmerle *et al*. [85], and Kraus *et al*. [86] provide practical guidelines for SIM sample preparation and data analysis, and also discuss artifacts generated during post-acquisition data processing.

SIM was used in the study of the sub-nucleolar localization of ALS-associated toxic dipeptide repeats and the associated changes in nucleolar morphology [31]. Parker and colleagues applied 2D and 3D SIM to study the core–shell architecture of stress granules and their assembly/disassembly kinetics [32, 34]. Multicolor SIM revealed that nuclear speckles (~1 μm in diameter) are sub-compartmentalized into compositionally distinct sub-speckles (Fig. 2a) [11]. Data from EM (described in the following section) had shown that these sub-speckles, which vary between 200 and 500 nm in diameter, exhibit sub-structural organization on the tens of nm length scale (reviewed in ref. [87]). Although these features cannot be resolved with SIM, they would be amenable to analysis with other super-resolution imaging methods, such as stochastic optical reconstruction microscopy (STORM), that achieve higher spatial resolution (down to tens of nm).

STORM provides the highest spatial resolution among super-resolution methods and can image sub-cellular structures with XY and axial resolutions of 10–20 and 10–75 nm, respectively, with temporal resolution of s to min [84]. STORM is based on sequential, sparse activation of photoswitchable fluorophores where super-resolution is achieved through precise determination (sub-nm accuracy) of the position of individual fluorophores. A high-resolution image is generated from multiple images of the same observation volume, which is repetitively illuminated to activate different sets of individual fluorophores [84, 88]. A maximum number of three different color fluorophores can be simultaneously imaged using STORM [84]. 2D and 3D STORM reconstructions were used to characterize the core–shell morphology of stress granules and their cores (~200 nm in diameter; Fig. 2b) in intact U2OS cells and cell lysates [32]. Special consideration (discussed in detail in refs. [89, 90]) should be given to the selection of photoswitchable fluorophores and to the fluorophore density in the specimen, the latter of which directly affects the maximum achievable resolution of the reconstructed image.

Lattice light-sheet microscopy (LLSM) marries the high-speed acquisition and optical sectioning of light-sheet microscopy with super-resolution technologies, to produce images with spatial resolution of 150–280 nm and sub-s temporal resolution, while minimizing photobleaching and phototoxicity [91]. Wang *et al*. [92] utilized 3D-SIM LLSM to demonstrate that the MEG-3 protein localizes to dynamic sub-compartments of P granules in *C. elegans* embryos. 4D LLSM was also applied to monitor formation, fusion, and dissolution of HP1α-containing liquid-like compartments at chromatin loci in live cells during cell cycle progression [36].

Complementary imaging methods are required to study the structural organization of molecules at even higher resolution within sub-μm, phase-separated cellular bodies, a prime example of which is EM.

Electron microscopy

EM employs a beam of accelerated electrons to illuminate fixed, contrast-stained samples and record images with spatial resolution as low as 0.8 Å in highly ordered structures [93]. Images are formed through deflection of electrons by electro-magnetic fields generated by atoms within the specimen. Transmission electron microscopy (TEM) uses fixed specimens that are negatively stained with heavy metal salts (i.e., uranyl acetate, tungsten or molybdenum salts, etc.) to image ultrastructural features of cells. The heavy metals preferentially bind the surfaces of biological structures, thus providing contrast to visualize organelles and their sub-structural features.

TEM has been used to study membrane-less organelles in cells such as the nucleolus [94, 95], nuclear speckles [87], Cajal bodies [30, 96], and RNP granules [97, 98], as well as macromolecular phase-separated assemblies formed *in vitro*, such as hydrogels and fibrils [99–101]. In order to obtain information on the localization and spatial distribution of specific components using TEM, samples can be immunoconjugated with colloidal gold particles coated with specific antibodies [93]. Souquere *et al*. [102] applied this technique to gain insights into the composition and preferred nuclear localization of CRM1- and intra-nucleolar bodies. The authors demonstrated that intra-nucleolar bodies, which are membrane-less bodies located within nucleoli, are enriched in SUMO-family post-translational modifiers, while the CRM1-nucleolar bodies are localized to the periphery of the nucleolus and are connected to the chromatin network [102].

Although high contrast can be achieved with negative staining in conventional TEM, cellular components can react differentially to staining agents, potentially resulting in unevenly labeled specimens. A modification of TEM, termed electron spectroscopic imaging, takes advantage of differential energy loss upon irradiation of naturally abundant elements (e.g., nitrogen and phosphorous) to distinguish nucleic acids and proteins in sub-cellular structures [103]. For example, Nott *et al*. [23] used electron spectroscopic imaging to determine that proteins and nucleic acids are relatively uniformly distributed

within Ddx4-containing organelles in HeLa cells, with 0.6 × 0.6-nm resolution in the XY plane.

Among the limitations of electron microscopy are the need to fix and process samples prior to imaging, preventing real-time monitoring of biological processes. The potential for radiation damage to the sample during data acquisition, and the risk of sample damage during the multiple steps of specimen preparation, also need to be considered [93].

Light microscopy and EM are often used as complementary methods to obtain insights into the structural and dynamic properties of cellular bodies [23, 30, 95–98]. New developments in accurate positional referencing of specimens on mounting grids, advances in the instrumentation, and the availability of software packages for cross-platform data correlation are the basis for correlated light and EM (CLEM). This allows both types of images to be obtained from the same sample. Using CLEM, a cellular sample is first analyzed using light microscopy and then processed for EM imaging. This requires using a shared positional reference, which provides the basis for direct correlation of light microscopy images with high-resolution ultrastructural information derived from EM [104]. Several studies have used CLEM to image the ultrastructure of nucleolar sub-compartments [105–107] and to track specific proteins found in cytoplasmic inclusions [108].

Changes in the ultrastructure of a membrane-less organelle, revealed using one or more of the imaging methods discussed above, are often associated with changes in molecular mobility and dynamics, the former probed using FRAP and FLIP, which in turn change the material properties of the organelle. Microscale rheology methods have been applied to characterize the viscoelastic properties of membrane-less bodies in live cells and *in vitro* and are discussed in the following section.

Rheology of Membrane-less Organelles

The material properties of membrane-less organelles (e.g., viscosity, surface tension, molecular network mesh size, etc.) and the dynamics of constituent molecules are likely to influence their biological functions and are altered in association with disease. Thus, determining the rheological properties of phase-separated bodies *in vitro* and in live cells is important in defining their physical state and has revealed fundamental principles that govern their internal architecture.

Membrane-less organelles exhibit increased macromolecular density and viscosity relative to the surrounding milieu. Determination of the density of macromolecules within phase-separated bodies was discussed in the section entitled Quantitative image analysis, above. The viscosity within these bodies is often quantified by measuring the diffusion coefficient of a fluorescently labeled component (e.g., using FRAP) and relating this to viscosity using the Stokes–Einstein equation (Eq. (6)). With this method, a few assumptions are made: (1) that the microenvironment within the droplet or organelle behaves as an equilibrium Newtonian liquid, and (2) that the hydrodynamic radius of the diffusing species is known or can be reasonably estimated [3]. A viscosity of ~1 Pa s was estimated for P granules based on the half-time of recovery in FRAP experiments using GFP-labeled PGL-1, with the assumption that the observable fluorescent molecules diffuse as a monomeric species [3]. It is well understood that proteins that localize to membrane-less organelles interact with other resident proteins and nucleic acids [9, 15, 25, 27], and often experience conformational compaction, especially of prevalent disordered regions, due to molecular crowding and the distinct physicochemical properties of the dense phase microenvironment [10, 27, 109, 110]. These factors, consequently, often alter the size of the diffusing species. An approach that avoids these complications is the use of inert particles that freely diffuse through the microenvironment of the dense phase.

Particle tracking microrheology (reviewed in ref. [111]) utilizes commercially available, fluorescently labeled nano- or micro-beads embedded within *in vitro* droplets. Importantly, the size and shape of the beads are uniform and well defined, and their surface is chemically modified (surface passivized) to prevent non-specific interactions with the components of the droplets. The mean-squared displacement (MSD; Eq. (7)), caused by thermal Brownian fluctuations in a viscoelastic medium, is quantified to calculate the diffusion coefficient of the particle (Eq. (8)) [111, 112]:

$$\mathrm{MSD}(\tau) = [x(\tau + t) - x(t)]^2 + [y(\tau + t) - y(t)]^2 \quad (7)$$

$$\mathrm{MSD} = 2D\tau^{\alpha} \quad (8)$$

where τ represents the time allowed for diffusion, α is the diffusive exponent, and x and y are the Cartesian coordinates of the particle. For a simple viscous liquid, $\alpha = 1$. The viscosity of the medium is obtained using the value of D determined using Eq. (8) and the Stokes–Einstein equation (Eq. (6)). This method was used to quantify the viscoelastic properties, such as viscosity and elasticity of the cytoskeleton and nucleoplasmic networks [111–113], as well as the viscosity of droplets formed *in vitro* with NPM1 [15] and LAF-1 (Fig. 3a) [25]. Brangwynne and colleagues correlated the diffusive exponent with the size of diffusing particles to gain insight into the dimensions of the mesh of molecular interaction networks within *Xenopus laevis* germinal vesicles [112] and *in vitro* droplets comprised of LAF-1 [14].

In addition to viscosity, another important parameter that characterizes the strength of molecular interactions in fluids is surface tension. Surface

tension is defined as the measure of the collective intermolecular forces that drive minimization of surface area in order to lower the interfacial energy between two liquids. The kinetics of fusion and relaxation reports on droplet viscosity and surface tension. Specifically, the ratio of viscosity (η) to surface tension (Υ), termed the inverse capillary velocity (η/Υ), is obtained from the slope of the linear relationship between the relaxation time and initial axial length scale of two fusing liquid-like bodies (Fig. 3b) [3, 4, 15, 25, 114]. Several types of manipulations, including the use of optical traps [37, 66, 115] and the application of sheer stress [3, 4], have been employed to increase the frequency of organelle or droplet encounters for improved statistics of quantitative analyses of fusion events. When the droplet viscosity is measured with one of the methods described above, the surface tension can be calculated from the inverse capillary velocity [25].

Another method to directly measure surface tension is through a right angle imaging approach, which allows quantification of time-dependent changes in the height of liquid-like bodies due to the force of gravity. This was used to determine the surface tension of *in vitro* liquid-like droplets and *Xenopus laevis* nucleoli within germinal vesicles; Eq. (9) describes the relationship between liquid-like body height and Υ [15].

$$\gamma = \frac{\Delta\rho g H^2}{4.308\left[1-\frac{H}{R}\right]} \qquad (9)$$

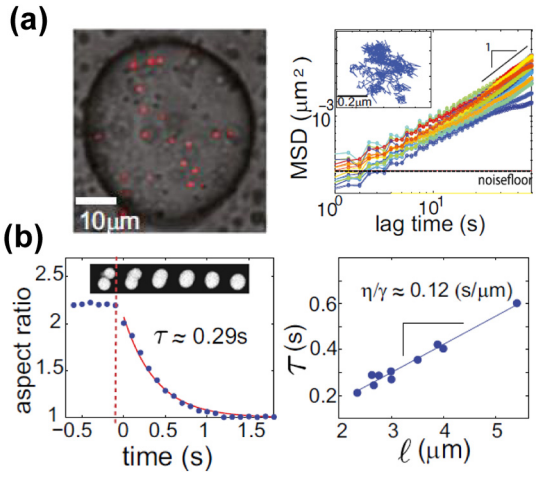

Fig. 3. Rheology of microscopic liquid-like bodies. (a) Determination of the viscosity of LAF-1 droplets using fluorescence micro-bead tracking; confocal microscopy image of beads embedded in the droplet (left) and the mean squared displacement *versus* lag time curves for the tracked beads (right). (b) Inverse capillary viscosity analysis to determine η/γ for LAF-1 *in vitro* liquid-like droplets: example of the relaxation curve for two coalescing droplets (left) and the linear plot of the relaxation time *versus* characteristic length scale (right). The figures were reproduced from Elbaum-Garfinkle *et al.* [25].

where R is the distance from the center of the object to its widest point, H is the height of the object, $\Delta\rho$ is the density difference between the dense and light phase, and g is the gravitational acceleration constant. Time-resolved 3D imaging can also be employed to determine surface tension, when appropriate deconvolution algorithms are applied to correct for distortions along the Z-axis [116].

Insights into the physiochemical properties of phase-separated bodies can be obtained by monitoring their interactions with surfaces of known chemical composition. Specifically, quantification of the contact angle of liquid-like droplets with surfaces of a known hydrophobic/hydrophilic character using 3D image reconstruction provides insights into the compatibility of the droplet internal microenvironment with the two chemically different types of surfaces [15]. For example, the observation of a low contact angle with a hydrophobic surface indicates that the interaction between the droplet microenvironment and the surface is energetically favorable due to like hydrophobicity. Correspondingly, a high contact angle would indicate energetically disfavored interactions between chemically incompatible hydrophilic droplets and the hydrophobic surface [15].

The morphology and physical features of membrane-less organelles depend on the nature and strength of inter-molecular interactions that drive their formation through phase separation, and these interlinked properties can be tuned in real time through time-dependent changes in organelle composition [55, 114]. This topic is discussed in the section below.

Compositional Characterization of Membrane-less Organelles

Most membrane-less organelles characterized to date are composed of proteins and nucleic acids, with incorporation of RNA observed more frequently than of DNA. Homotypic [23, 25, 27, 117] or heterotypic [9, 15, 25] interactions involving proteins and/or RNA can drive phase separation. Whether *via* a nucleating event or spontaneous demixing, a complex network of interactions is established within the resulting membrane-less organelle [27, 54], thereby defining its unique protein and RNA content. Early studies that addressed organelle composition utilized immunofluorescence and fluorescence *in situ* hybridization (FISH) techniques [118–121]. While informative, these methods are low throughput and often require prior knowledge of the system under study. Unbiased, large-scale methods have been applied to broaden our understanding of the biomolecular composition of a variety of different membrane-less organelles, as discussed below.

Proteomics

High-throughput, mass spectrometry-based methods are ideally suited for analyzing the composition of complex biomolecular mixtures isolated from cells with high signal-to-noise ratios and sensitivity. In particular, these methods have allowed comprehensive analyses of protein–protein interaction networks [122, 123]. Membrane-less organelles are fluid, environment-responsive cellular bodies that dynamically assemble and disassemble, making their isolation challenging. The first insights into the proteome of a membrane-less organelle, the nucleous, were obtained in 2002 by Andersen and colleagues [124], who coupled nuclear fractionation with mass spectrometry to identify the nucleolar proteome. In the initial study, the authors used a combination of 1D and 2D SDS-PAGE, MALDI-TOF and nano-electrospray technologies to identify 271 nucleolar proteins [124]. Through technological advances in mass spectrometry methods, which improved signal-to-noise ratios, and improvements in bioinformatics analysis methods, the known nucleolar proteome has expanded to now include 4500 proteins [125].

Intact nucleoli [4, 71, 124–126] in these studies were purified by density gradient fractionation, taking advantage of their high density relative to other cellular bodies. Interestingly, ATP is required for nucleolar dynamics [4]; removal of ATP causes nucleoli to lose their liquid-like character, while preserving their structural integrity [4]. These physical changes can be exploited in the fractionation protocol, preventing nucleolar coalescence during the centrifugation steps, allowing the isolated nucleoli to maintain their size, shape, sub-compartmentalization and transcriptional activity *in situ* [71]. Nucleolar morphology and protein content dynamically change in response to various types of cellular stress (reviewed in ref. [127]). Changes in the nucleolar abundance of 489 human proteins were quantitatively analyzed in nucleoli extracted from cells that were stressed with transcription (actinomycin D) and proteasome (MG132) inhibitors, by coupling stable-isotope labeling by amino acids in cell culture (SILAC) with cellular fractionation and LC–MS/MS [71]. Here, the authors showed that the levels of ribosomal proteins inside nucleoli decreased upon treatment with actinomycin D and increased upon treatment with MG132 [71], illustrating how different types of stress signals are translated into changes in the compositional and likely, also the biophysical properties of a membrane-less organelle.

Unfortunately, due to their liquid-like properties, not all membrane-less organelles can be isolated in intact form through cellular fractionation. For example, stress granules exhibit a core–shell architecture, with a stable core and labile shell. The core can be enriched and isolated, while the labile shell is lost during isolation procedures [32]. The proteome of stress granule cores in yeast and human cells was characterized by coupling cell fractionation of stressed cells with affinity purification and LC–MS/MS. The human stress granule core proteome was found to be composed of 317 and 228 proteins, in the presence and absence of a cross-linker, respectively [32]. Bioinformatics analysis revealed that ATP-dependent helicases and protein remodelers are conserved components of stress granule cores in yeast and mammals [32]. This method further enabled the identification of additional, novel protein components of stress granule cores.

An alternative approach, the BioID method, was used by Youn *et al*. [128] to characterize the proteomes of P-bodies and stress granule subcompartments. In BioID, an abortive ligase tag (BirA*) is fused to a protein of interest (bait), which catalyzes biotinylation of polypeptides that are within ~10 nm of the bait [129]; the proximal, labeled proteins are then identified using mass spectrometry [128]. Using 119 individual bait proteins, the authors identified 7424 unique proximity-based interaction sites within 1792 prey proteins, 144 of which were assigned as core proteins in stress granules and P-bodies. Interestingly, this study revealed that the core proteins exhibit pre-existing proximity interactions under non-stressed conditions, which may serve as seeds for formation of stress-induced, microscopic granules [128].

Proteomics methods have been used to identify the sub-cellular compartments targeted by toxic, arginine-rich di-peptide repeat polypeptides (DPRs) associated with certain neurodegenerative diseases [130]. Immunoprecipitation of GFP-labeled DPRs coupled with LC–MS/MS analysis showed an association of the toxic polypeptides with RNA-binding proteins and proteins containing low-complexity (LC) domains. Many of the identified proteins are associated with several types of membrane-less organelles [31].

Because large-scale identification of protein composition requires isolation of intrinsically labile membrane-less organelles, the reported proteomes are likely incomplete due to the loss of weakly associated components. Chemical or UV cross-linking can be used to capture weakly associated components. As noted above, the composition and morphology of many membrane-less organelles are intrinsically dynamic. For example, nucleoli disassemble and reassemble during cell division, and stress granules rapidly form in response to stress stimuli, presenting challenges for their isolation and characterization of their components in specific functional states. Therefore, these features and associated limitations should be taken into account when interpreting proteomics results from membrane-less organelles. Additional, complementary experiments are often required to validate

findings from proteomics studies. Despite these limitations, proteomics studies have provided a wealth of information on the composition, function, and dynamic properties of membrane-less organelles. Based on the success of the studies on the nucleolus and stress granules, we anticipate that this technology will be soon applied to gain insights into the diverse protein components of other, less well-understood membrane-less organelles. In addition to containing specific sets of proteins, specific RNA species (reviewed in ref. [131]) also contribute to the unique molecular identities of membrane-less organelles, as discussed in the next section.

Transcriptomics

The RNA composition of stress granule cores discussed above was also determined using modified isolation procedures by Khong *et al.* [132]. After isolation, the RNA fraction of the cores was quantitatively analyzed using RNA-Seq, and further validated using single-molecule FISH [132]. The results indicated that in yeast and human cells, ~80% of the transcriptomic composition of stress granule cores is mRNA, with some enrichment in long intergenic noncoding (linc-) and noncoding (nc-) RNAs. The identities of the mRNAs incorporated within stress granule cores were determined using RNA-Seq and their enrichment was quantified using single-molecule FISH. While no preference for the transcripts of specific genes, or sets of genes, was observed, stress granules were enriched in long transcripts and those with long 5′ untranslated regions. A total of ~42,000 RNA molecules were incorporated into stress granule cores, including ~9000 ncRNAs and ~33,000 mRNAs [132]. The results of this transcriptomic analysis support the hypothesis that stress granules form by condensation of mRNAs of inefficiently/poorly transcribed genes and/or long mRNA molecules not actively undergoing translation [132]. Notably, under conditions of endoplasmic reticulum stress, only a sub-set of translationally suppressed mRNAs, with roles in cell proliferation and survival, and which displayed AU-rich sequence motifs, was targeted to stress granules [133]. These results by Namkoong *et al.* [133] support the idea that transcripts are specifically targeted to stress-induced granules.

Advances in our understanding of the proteomic and transcriptomic composition of membrane-less organelles require development of new and adaptation of existing methodologies to address the dynamic nature of these systems. For example, spatially targeted optical microproteomics (STOMP) [134], a method that uses two-photon laser scanning microscopy to photochemically cross-link an affinity (poly-histidine) tag to proteins within a well-defined ROI ($< 1\ \mu m^3$ volume) in cell or tissue samples, could be applied to purify and identify the proteomes of small membrane-less organelles in cells. Classic fluorescence activated cell sorting was adapted by Hubstenberger *et al.* [135] to purify endogenous P-bodies from cell lysates, based on detection of a fluorescently labeled reporter protein within particles and particle size. Proteomic and transcriptomic analysis of the sorted particles revealed that specific protein:protein and protein:RNA interactions regulate the condensation of specific mRNP complexes within P-bodies. Upon P-body condensation, the bound mRNAs did not undergo degradation or decapping, consistent with a functional role of dynamic mRNA reservoirs in the cells, thus allowing them to easily re-enter translation upon P-body dissolution and, in turn, influence gene expression in the cell [135].

The material properties and composition of membrane-less organelles are intimately related to the physicochemical nature of the interactions that define the molecular network within the dense phase of the demixed solution (e.g., hydrophobic, electrostatic, π–π interactions), and likely control organelle function. The methods that characterize structural (Å to sub-μm length scale) and dynamic (ps to s) features of these networks are discussed in the following section.

Structural Characterization of Molecular Networks within Membrane-less Organelles

A steadily growing body of literature has established that proteins with regions of low amino acid sequence complexity have a high tendency to undergo phase separation. LC regions often exhibit multiple repeats of sequence elements that experience weak self-association and mediate both intra-molecular and inter-molecular protein interactions. These types of multivalent interactions within and between LC protein regions are the basis for the formation of molecular networks with interactions on the Å to tens of nm length scales. The presence of multiple, folded interaction domains can also drive multivalent interactions and phase separation [9]. Many proteins that undergo phase separation contain both folded domains and LC regions. Importantly, the amino acid composition and sequence patterns of LC regions often disfavor the formation of secondary or tertiary structure and, correspondingly, are associated with conformational disorder, presenting challenges for structural characterization using structural biology techniques best suited for folded proteins.

The lack of stable secondary and tertiary structure and extensive conformational dynamics inhibit the formation of ordered arrays of molecules required for crystallization and limit the use of X-ray crystallography for atomic resolution analysis of LC protein

regions and their phase-separated bodies. For similar reasons, cryo-EM (cryo-EM), which relies on samples that exhibit compositional and structural homogeneity that are "frozen out" for EM imaging, is poorly suited for analysis of conformationally heterogeneous LC domains. In contrast, NMR spectroscopy, which has been widely used for decades in studies of intrinsically disordered proteins (IDPs) [136], is well suited for the analysis of the structural and dynamic features of disordered LC protein regions. However, low sequence complexity is associated with poor resonance dispersion and intra- and inter-molecular multivalent interactions, often leading to phase separation, reduced rotational, and translational motions, and causes resonance broadening; all of these factors present challenges for NMR studies of LC regions at atomic resolution. Despite these limitations, several techniques described in the following sections, have been applied to study the structural and dynamic properties of proteins with LC regions, before and after phase separation (Fig. 4).

NMR spectroscopy

NMR exploits the properties of atoms that exhibit non-zero nuclear spin (most commonly with spin quantum number, *I*, *of* ½). For biomolecular NMR, the nuclei of interest with $I = ½$ include ^{1}H, ^{13}C, ^{15}N, ^{19}F, and ^{31}P. While the ^{1}H, ^{19}F, and ^{31}P isotopes are naturally highly abundant (99.99%, 100%, and 100%, respectively), the natural abundance of the spin ½ nuclei for nitrogen and carbon are 0.37% and 1.07%, respectively [137]. To address the latter isotopic deficiencies, recombinant proteins are expressed in bacteria grown in isotopically enriched media to achieve uniform incorporation of NMR-detectable isotopes for the nuclei of carbon and nitrogen atoms. While isotopic enrichment significantly enhances sensitivity, NMR is an intrinsically insensitive technique and concentrations of isotopically labeled proteins and other biopolymers above ~10 μM are required even with the most sensitive of NMR spectrometers, for example, those equipped with high-field magnets and cryogenically cooled detection probes.

Analysis of protein structural features using NMR spectroscopy

Residue-specific chemical shift values (termed δ) of nuclei for polypeptide backbone atoms (e.g., $^{1}H_N$, $^{15}N_H$, $^{13}C'$, and $^{13}C_\alpha$) report on the population of secondary structure (α-helix or β-strand) and so-called random coil conformations and are sensitive reporters of the local chemical environment ($^{1}H_N$ chemical shift values are particularly sensitive). Therefore, changes in chemical shift values (termed chemical shift perturbations, or CSPs) due to, for example, enhanced protein interactions associated with phase separation, are residue-specific reporters of the sites of, and any conformational changes associated with, these interactions. CSP analysis has been applied to map interaction sites within LC domains of several proteins that undergo phase separation [16, 117, 138]. Analysis of secondary chemical shift values (termed Δδ), corresponding to differences between experimental chemical shift values and standardized values for "random coil" conformations, identifies regions with preference for secondary structure (non-zero values), or the absence thereof (near zero values), and reports on changes in conformation due to, for example, phase separation. This type of analysis showed that a helical element in the C-terminal LC region of the protein TDP-43, a component of RNP-granules, is required for phase separation *in vitro* [117]. Interestingly, application of the same type of analysis to the LC region of FUS [16] (Fig. 4b, c), one of the acidic tracts of the nucleolar protein NPM1 [138], and the RGG domain of the Ddx4 RNA helicase [10], showed that, while engaged in multivalent interactions, these protein regions maintained disordered conformations (lacking secondary structure) within phase-separated bodies *in vitro*. When coupled with titration experiments, the magnitude of CSPs can be analyzed to extract residue-specific dissociation constants [138].

Poor resonance dispersion for residues within LC regions can limit the types of detailed analyses discussed above, especially for proteins with multiple folded domains and/or intrinsically disordered regions (IDRs). This limitation can be addressed using selective isotopic labeling of IDRs within proteins, although this requires specialized protein ligation techniques [139]. Alternatively, resonance dispersion for IDRs can be improved using spectral editing techniques [140] and spectral resolution can be improved using direct detection of ^{13}C or ^{15}N nuclei [140–142].

The nuclear Overhauser effect (NOE) reports on through-space magnetization transfer *via* dipole–dipole interactions, which exhibit r^{-6} length dependence (where *r* is the distance between two spin ½ nuclei). In the case of ^{1}H nuclei, homonuclear ^{1}H–^{1}H NOE enhancements are observed for *r* values less than 6 Å. Recently, Brady *et al.* [10] used ^{13}C-filtered, ^{13}C-edited ^{1}H–^{1}H NOE spectroscopy experiments to study short-length scale interactions between specific types of amino acids in the LC region of Ddx4 before and after phase separation *in vitro*. While resonances of individual amino acids could not be resolved due to low sequence complexity, NOE enhancements were observed between groups of arginine and phenylalanine residues, providing insight into the inter-residue interactions that underlie molecular network formation and phase separation by Ddx4.

A complementary method involves measurement of paramagnetic relaxation enhancements (PREs;

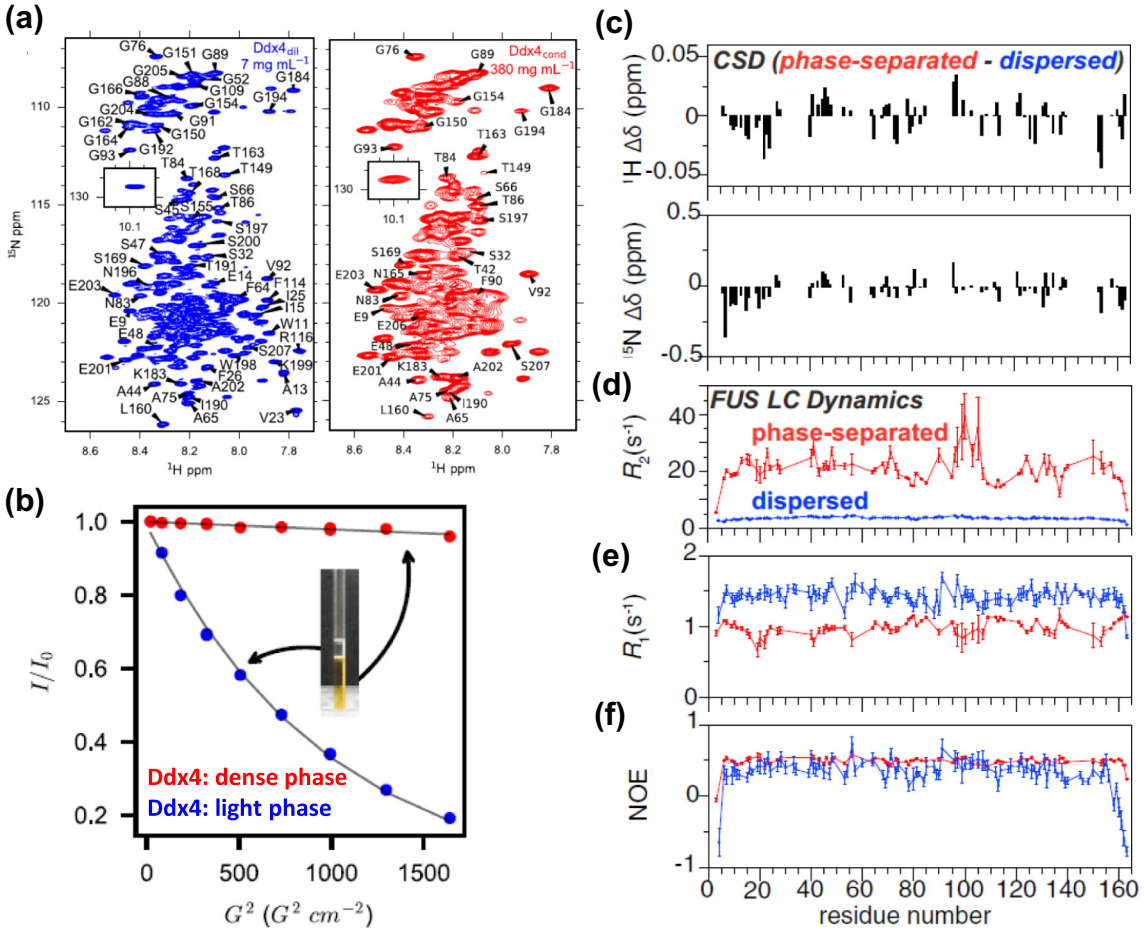

Fig. 4. NMR-based techniques used for characterization of phase separation-prone proteins. (a) The 2D $^{1}H/^{15}N$ heteronuclear single quantum coherence spectrum of Ddx4 N-terminal domain (blue) exhibits resonance broadening upon demixing (red). (b) PFG determination of molecular diffusion for Ddx4 in the light (blue) and dense (red) phases. Panels a and b were reproduced from Brady *et al.* [10]. (c–g) Residue-specific characterization of FUS LC domain structure and dynamics prior to demixing (blue) and within the dense phase of a demixed solution (red), by ^{1}H and ^{15}N CSPs (c) and by R_2 (d), R_1 (f) relaxation, and heteronuclear NOE, respectively. Panels c–f were reproduced, with permission, from Burke *et al.* [16].

see Analysis of protein dynamics using NMR spectroscopy section for more details) due to dipole–dipole interactions between nuclei and the unpaired electron of a paramagnetic spin label. PREs are used to map interaction between nuclei (usually backbone HN groups) throughout a protein and specific residues (usually native or engineered Cys residues) that are covalently conjugated to a paramagnetic spin label, such as MTSL with a nitroxide group. Since site-specific conjugation is required for PRE measurements, successive Cys mutagenesis is often performed to map the entire amino acid sequence. Spectra collected with the paramagnetic spin label are compared with the corresponding spectra collected with protein in which the spin label is chemically reduced, making it diamagnetic, and thus eliminating PRE effects. Because the magnetic moment of the unpaired electron of the nitroxide group is very large, PRE reports on longer distances compared to $^{1}H–^{1}H$ NOE enhancements, up to ~35 Å. The PRE method was used to demonstrate that inter-molecular interactions between the helical segment within the C-terminal LC region of TDP-43 drive phase separation [117]. By contrast, PRE analysis of the FUS LC showed predominantly non-specific intra- and inter-molecular interactions, consistent with a collapsed ensemble of disordered conformations in solution and retention of structural disorder in the phase-separated state [79]. Due to the requirement of site-specific labeling, which often is accompanied by site-directed mutagenesis, it is important to understand the effect the point mutation(s) and chemical labeling have on protein structure and interactions through performance of appropriate control experiments.

Analysis of protein dynamics using NMR spectroscopy

NMR is among the few techniques capable of providing residue-specific information on molecular dynamics. The most direct measure of dynamics is the resonance lineshape, whose width is proportional to the transverse relaxation rate R_2 (Eq. (10)), thereby reporting on residue-specific dynamics:

$$\Delta\nu_{FWHH} = 1/(\pi T_2) = R_2/\pi \qquad (10)$$

where $\Delta\nu_{FWHH}$ is the full-width at half-height of the Lorentzian lineshape, T_2 is the transverse relaxation time, and R_2 is the transverse relaxation rate. R_2 values report on motions on the ps to ns timescale but are also influenced by conformational fluctuations on the μs to ms timescale. Broadening of ^1H_N resonances was observed in association with homotypic phase separation of the LC regions of Ddx4 (Fig. 4a) [10] and FUS [16], as well as with heterotypic phase separation of the pentameric, N-terminal region of NPM1 with a peptide derived from the ribosomal protein rpL5 [138], due to slowed molecular motions in the protein-rich dense phases and/or as a result of site-specific protein–protein interactions. While often straightforward to measure (a non-standard method was used in the case of NPM1/rpL5 [138]), the interpretation of resonance broadening is often complicated by multiple contributing factors, including conformational exchange and sample heterogeneity (e.g., the presence of multiple oligomeric forms of the protein of interest in equilibrium with phase-separated bodies, as well as heterogeneity within the dense phase), the latter of which is of particular concern for phase-separated samples.

Pulse field gradient (PFG) NMR is used to determine diffusion coefficients and is useful in the analysis of complex mixtures, where resonances of different species can be separated on the basis of molecular size [10, 23, 27]. During PFG experiments, resonances exhibit intensity attenuation (neglecting relaxation effects) that depends on the protein diffusion coefficient (which is a rate) and the duration and strength of the applied field gradient; little attenuation is observed for large, slowly diffusing proteins, while extensive attenuation is observed for small, rapidly diffusing proteins. The resulting decay curves, plotted as a function of normalized intensity *versus* gradient field strength (keeping duration constant), are fit to extract the diffusion coefficient (Eq. (11)),

$$\ln\frac{I}{I_0} = -DY^2g^2\delta^2\left(\Delta - \frac{\delta}{3}\right) \qquad (11)$$

where I and I_0 are the gradient-influenced and reference (with no gradient applied) signal intensities, respectively, D is the diffusion constant, Υ is the ^1H gyromagnetic ratio, g is the gradient strength, δ is the duration of the gradient, and Δ is the duration of the evolution period. The diffusion coefficient can be converted into the hydrodynamic radius by applying the Stokes–Einstein equation (Eq. (6)). PFG NMR is ideally suited for determining diffusion coefficients of small molecules or proteins that have small transverse relaxation rates.

Using a ^{15}N-filtered PFG experiment, Mitrea *et al.* [27] observed weak interactions between acidic and basic regions within the IDR of NPM1, providing a mechanism for inter-molecular NPM1 interactions associated with homotypic phase separation. It should be noted that the signal attenuation observed in PFG NMR experiments scales exponentially with the diffusion coefficient, thus for phase-separated systems in which molecules may diffuse much more slowly than in monodisperse solutions due to increased viscosity and quinary interactions, the measurement of diffusion coefficients may not be possible using traditional methods. To circumvent this limitation, Kay and colleagues developed a methyl group triple-quantum PFG experiment which enhances the effective gradient strength by 3-fold. Application of this method revealed that the N-terminal LC region of Ddx4 experiences a nearly 100-fold reduction in the rate of translational diffusion upon phase separation (Fig. 4g) [10]. Furthermore, diffusion coefficients were measured for several small probe molecules and proteins diffusing within phase-separated Ddx4 and showed that translational diffusion slowed as a function of apparent R_h, consistent with excluded volume effects by the Ddx4 molecules in the scaffold of the dense liquid phase [10].

Measurements of the longitudinal (R_1) and transverse (R_2) relaxation rates, and heteronuclear NOE enhancements, referred to collectively as nuclear spin relaxation techniques, probe protein dynamics on the ps to ns timescale, providing information on bond vibration/libration, side-chain rotamer reorientation, and backbone torsion angle rotation [10, 16, 78, 101, 117, 143]. Nuclear spin relaxation has been applied to the LC domains of FUS [16] (Fig. 4d–f), hnRNPA2 [78], and Ddx4 [10]. These examples demonstrated that while these LC domains retain conformational disorder in the phase-separated states as indicated by small CSPs, increased transverse relaxation rates were observed upon phase separation, indicating that molecular motions were restricted in these protein dense phases. Interestingly, slightly increased transverse relaxation rates were also observed for a concentrated solution of the $Ddx4_{14FtoA}$ mutant, which does not undergo phase separation, suggesting that, in addition to transient protein–protein interactions, increased solution viscosity also affects the observed backbone dynamics of Ddx4 in the phase-separated state.

Relaxation dispersion methods provide kinetic, thermodynamic, and structural information on

chemical exchange processes that occur on the µs to ms timescale. Carr–Purcell Meiboom–Gill ^{15}N relaxation dispersion and $R_{1\rho}$ relaxation dispersion probe chemical exchange processes with values of k_{ex} ($k_{ex} = k_{forward} + k_{backward}$ for two-state exchange) $\leq 10^4$ s^{-1} [117, 144] and $k_{ex} \leq 10^5$ s^{-1} [144], respectively. Carr–Purcell Meiboom–Gill relaxation dispersion measurements demonstrated that TDP-43 monomers exist in equilibrium with higher-order oligomers and were used to quantify the exchange rate and the relative populations of the two species [117]. Slow exchange rates and very small chemical shift differences ($\Delta\omega$) between the exchanging states often characterize disordered proteins within highly concentrated phase-separated bodies, limiting the application of classical relaxation dispersion methods. For such cases, an off-resonance ^{15}N $R_{1\rho}$ method has been used to derive a complete set of exchange parameters for phase-separated Ddx4, a system that exhibited $\Delta\omega \approx 0$ and minimal changes in R_2 values [144].

Dark-state exchange saturation transfer experiments permit the transfer of magnetization from lowly populated and transient, NMR-invisible states (e.g., a high-molecular-weight ligand-bound state of a protein) to a highly populated detectable species (e.g., the low-molecular-weight unbound state of a protein) through chemical exchange. This provides residue-specific information for exchange processes on the 10-ms to 1-s timescale and can be used to extract k_{on} and k_{off} rates for systems that exhibit two-state exchange [101]. A particular advantage of this method is that it relies on changes in relaxation rates between the two states, and not on CSPs [101, 144], and therefore is more amenable to analysis of disordered proteins and their phase-separated states. The dark-state exchange saturation transfer was applied to gain atomic-level dynamic insights into the interaction between the C-terminal disordered domain of RNA Pol II in complex with fibrils formed by the LC domains of two RNP granule-associated proteins, hnRNPA2 and TAF15 [101].

Solid-state NMR spectroscopy

In addition to forming liquid-like, phase-separated bodies, many LC regions have been shown to form hydrogels *in vitro*. The semi-solid nature of these assemblies enables use of solid-state NMR (ssNMR) methods to study their structural and dynamic features. The achievable resolution using ssNMR is limited by resonance broadening and generally requires samples with a high degree of intrinsic order, and dynamics which are either negligible or very fast (e.g., on the ps timescale). Resonance broadening is often reduced through sample crystallization or directed labeling strategies. Despite these limitations, advances in ultra-high-field NMR instruments, ultrafast magic angle spinning probes, and NMR methodology, enable the application of ssNMR techniques to biomolecules of increasing size and complexity, including proteins that undergo phase separation. Renault *et al*. [145] provide an extensive review of biomolecular ssNMR.

In a recent study, Dannatt *et al*. [146] showed that *E. coli* single-stranded DNA binding protein readily forms hydrogels *in vitro*. Using ssNMR methods to measure CSPs and ^{15}N $R_{1\rho}$ values showed that the C-terminal acidic motif transiently interacts with the DNA binding groove, thus rationalizing the observed hydrogelation and providing a mechanism for the observed auto-inhibition [146].

Reichheld *et al*. [143] applied a combination of solution- and solid-state NMR techniques to monitor the structure and dynamics of an elastin-like polypeptide (ELP) in solution, as a coacervate, and as a cross-linked elastomeric material. The authors found that the ELP experienced a reduction in both local dynamics and global diffusion upon transitioning from the solution to coacervated and cross-linked states. Importantly, the ELP exhibited predominantly disordered conformations in each phase, highlighting the relationship between conformational entropy and the elastomeric properties of elastin polymers.

Murray *et al*. [80] applied a range of solid-state magic angle spinning NMR techniques to elucidate the molecular structure of fibrils formed by the FUS LC region. Interestingly, the resulting structural model revealed a fibril core formed by 57 residues within the N-terminus, while other regions of the LC region remained disordered. The fibril core exhibited a single cross-β unit, whose conformation was similar to that observed for α-synuclein. Strikingly, the FUS LC region fibril core was stabilized by an abundance of intra-molecular and inter-molecular hydrogen bonding and dipole–dipole interactions mediated by polar side chains. These interactions are distinct from the hydrophobic interactions that stabilize fibrils formed by α-synuclein and amyloid-β [80] and may explain the ability of hydrogels comprised of FUS fibrils to dissolve under certain conditions [99, 147] (see below, in the *X-ray diffraction* section).

Together, these examples demonstrate the utility of NMR techniques for elucidating the molecular determinants of protein phase separation and the structural features of proteins within phase-separated bodies, be they liquid-like or hydrogels, at atomic resolution. Solution NMR methods can also probe the dynamics of proteins within various types of liquid-like and other mesoscale assemblies on timescales from ns (e.g., amide bond fluctuations) to µs and ms (e.g., conformational exchange and translational diffusion) to s (e.g., slow association/dissociation events). Finally, ssNMR methods enable the structural characterization of proteins within hydrogels and fibrils, physical states at the far end of the disorder-to-order continuum associated with phase separation.

X-ray diffraction

X-ray diffraction is applied to characterize the structural features of a range of materials, including fluids, minerals, and polymers. The X-ray diffraction pattern provides a fingerprint of periodic atomic arrangements in a given material [148] and has been used extensively for the structural characterization of amyloid fibers, which comprise repeating intermolecular β-sheets—termed "cross-β-sheets." This structural arrangement produces characteristic X-ray fiber diffraction patterns, with reflections at ~4.8 and 6–12 Å, which correspond to the spacing between β-strands and the distance between stacked β-sheets, respectively [149, 150]. Importantly, LC regions from some proteins associated with membrane-less organelles can undergo phase separation to form hydrogels *in vitro*. X-ray diffraction studies of hydrogels formed by these LC regions (i.e., from FUS, hnRNP A2, nucleoporins, etc.) have revealed diffraction patterns consistent with cross-β structure [99, 100, 151].

Although morphologically similar to pathogenic, prion-like amyloids, the fibers formed from the noted LC regions readily disassemble upon treatment with SDS or aliphatic alcohols, heating, or dilution [99, 100, 147, 151]. Due to the inherent heterogeneity of these hydrogels, the X-ray diffraction data could not be used for atomic resolution structure determination. However, taking advantage of the repetitive nature of the interaction motifs, Hughes *et al*. [150] used X-ray crystallography to determine high resolution (~1 Å) structures of five segments derived from LC regions of proteins that undergo phase separation, including FUS, hnRNP A1, and NUP98. Their structures revealed a common structural motif consisting of pairs of kinked β-sheets, which interacted weakly through polar atoms and aromatic side chains, thus distinguishing them from the steric zipper configurations exhibited by amyloid fibrils [150]. The atomic-resolution information obtained for these structural motifs can be coupled with complementary structural methods that provide insights on longer length scales, as well as with computational methods, to more fully understand the structural mechanisms that underlie phase separation by LC regions and other protein domains within membrane-less organelles.

Cryo-EM and tomography

Cryo-EM and cryo-electron tomography (cryo-ET) provide structural information on the Å to nm length scale and can be used to study biomolecules in their native cellular environment. Cryo-EM/ET thus enable access to structural information on length scales between light microscopy and more traditional structural biology techniques, such as X-ray crystallography and NMR spectroscopy. Cryo-EM/ET can be performed on a wide range of samples, including purified macromolecular complexes, cells, tissues, or organisms. With cryo-EM, 10 to 100 s of thousands of electron microscopy images of individual but identical particles, which assume different orientations on a 2D grid surface, are computationally combined to construct the 3D structure of the particle (e.g., a multicomponent protein assembly). In cryo–ET, many images of a single object (e.g., a thin section of a cell) are recorded with different electron beam tip angles, and the resulting projections are aligned and mathematically combined to construct a 3D image of the object. Cryo-EM has received little application in studies of phase-separated systems due to the requirement for homogeneous particles, but may prove useful in studies of soluble oligomers associated with nucleation of phase transitions in the future. In contrast, cryo-ET holds great potential to provide insight into the structural organization of biomolecules within mesoscale phase-separated bodies. For example, cryo-ET was used to characterize gel-like droplets formed by Sup35. The 3D-rendered volume revealed a well-defined, but disordered, meshwork of protein cross-links with an average mesh size of ~10 nm [37]. The maximum resolution for *in situ* cryo-ET is limited by sample thickness. Samples thicker than 300 nm can significantly blur images and reduce the overall resolution [152]. Advances in sample preparation, such as focused ion beam (FIB) milling methods (described in detail in ref. [152]), enable precise, region-specific milling to give lamella as thin as 170 nm, allowing cryo-ET analysis of cellular structures of interest [152, 153]. The FIB milling process can be guided by correlated 3D fluorescence light microscopy, allowing cryo-ET studies of specific regions within complex cellular structures [152]. FIB milling methods were applied to characterize the structures of polyglutamine (polyQ)-expanded huntingtin exon 1 inclusions in cells, and offers great potential for understanding the detailed architecture of membrane-less organelles in the future [153].

The structural insights obtained using X-ray diffraction, NMR spectroscopy, and cryo-EM/ET, are well complemented with light scattering methods, as discussed next.

Scattering methods

Scattering of electromagnetic radiation of different wavelengths can provide insights into the structure and organization of macromolecules in solution, on the tens of Å to μm length scale [154]. Mathematically, scattering of electromagnetic radiation is described by Eq. (12):

$$q = \frac{4\pi n}{\lambda} \sin\left(\frac{\theta}{2}\right) \tag{12}$$

where q is the magnitude of the scattering vector, n is the refractive index of the solvent, θ is the scattering angle, and λ is the wavelength of the incident light. Scattering methods provide information on large-scale conformational changes, oligomerization, and macromolecular complexation. Sample homogeneity is crucial for optimal data acquisition, depending on the application, as mixed populations can yield convoluted results. The ability to deconvolute contributions from multiple species is dependent on the timescale of interconversion and the resolution of the technique. In studies of membrane-less organelles, scattering methods have been used to determine phase diagrams for formation of protein:protein and protein:RNA phase-separated bodies, characterize correlation distances within phase-separated bodies, and quantify changes in protein and nucleic acid chain compaction [27, 138, 155].

Solution turbidity

Phase boundaries for protein and/or RNA systems can be determined by detecting changes in solution turbidity using a turbidity meter, nephelometer, or spectrophotometer. Solution turbidity is measured at fixed wavelengths outside the wavelength range of a normal protein absorbance spectrum [15, 117, 138, 156, 157] ($\lambda > 320$ nm; for a comprehensive review, see ref. [158]). Ishimoto and Tanaka [159] were among the first to adapt this method to the study of protein phase separation through the analysis of aqueous solutions of lysozyme and NaCl, demonstrating a concentration threshold of mixing/demixing. Turbidity measurements were subsequently used to demonstrate protein phase separation as the mechanism underlying cold cataract formation in the optical lens [160].

Solution turbidity can be used to determine concentration thresholds for phase separation as the concentration(s) of one or more components of a system are varied. Similarly, the temperature dependence of phase separation can also be monitored. For example, Quiroz and Chilkoti [156] used solution turbidity to quantify the upper and lower critical solution temperatures (UCSTs, LCSTs) of disordered repeat peptides with variable amino acid composition and demonstrated selective tunability of phase separation thresholds through changes in motif length and in the physicochemical properties of the constituent amino acids (Fig. 5a).

Turbidity was used to determine the relative charge fraction of mixed supercharged macromolecules required to induce phase separation *via* a charge neutralization mechanism [157] and the dependence of the saturation concentration for phase separation of supercharged GFP mutants [157] and IgG1 antibody [162] on environmental conditions such as temperature, salt, and pH. The concentration thresholds for homotypic [27] and heterotypic [15, 27, 138] phase separation involving the nucleolar protein NPM1, as a function of component concentration, were determined by monitoring solution absorbance at 340 nm. Turbidity assays coupled with domain deletion and site-directed mutagenesis enabled the elucidation of the structural features of NPM1 required for phase separation [15, 27, 138].

Turbidity measurements are non-destructive and thus can be coupled with UV absorbance measurements to quantify component concentrations within the dense and light phases after demixing *via* centrifugal partitioning [157]. When coupled with automated liquid handling devices and microplate readers, this method can be adapted for high throughput [163, 164]. It is important to appreciate that an increase in solution turbidity can be attributed to various phenomena including phase separation into dense liquids, hydrogels or solid particles, or non-specific protein aggregation. Thus, turbidity measurements should be coupled with complementary imaging studies to assess the physical properties of the phase-separated bodies (see above).

Light scattering

Several methods, including dynamic light scattering (DLS), static light scattering (SLS), and multi-angle light scattering, are used to analyze particle size and shape over a large range of molecular weights and hydrodynamic radii (MW ~300 Da–1 MDa; R_h ~0.2 nm–3 μm) (reviewed in refs. [154, 165, 166]). Light scattering methods are non-destructive, allowing samples to be used for additional experiments.

DLS measures time-resolved fluctuations in the intensity of scattered light observed at a specified angle [165, 166]. DLS has been used to detect formation of large oligomers and determine the saturation concentrations for phase separating proteins [9, 155]. The reversibility of LLPS in mAb solutions was demonstrated by comparing DLS profiles obtained in monodisperse conditions and after dilution of demixed samples into the single-phase, monodisperse, concentration regime [167].

The binodal and spinodal curves of phase-separated systems can be characterized by combining of DLS and SLS. In the study of phase-separated systems of elastin-like proteins [168], DLS was used to determine the binodal curve (metastable region) of the phase diagram by monitoring changes in the hydrodynamic radius of soluble complexes and SLS measurements were used to define the spinodal curve (unstable/demixed region) [168]. Here, the reciprocal of the measured scattered intensity was plotted as a function of temperature and the spinodal temperature was determined by extrapolation to infinite scattering intensity. DLS and SLS were also used to gain insights into YCl_3-induced phase separation of BSA and the

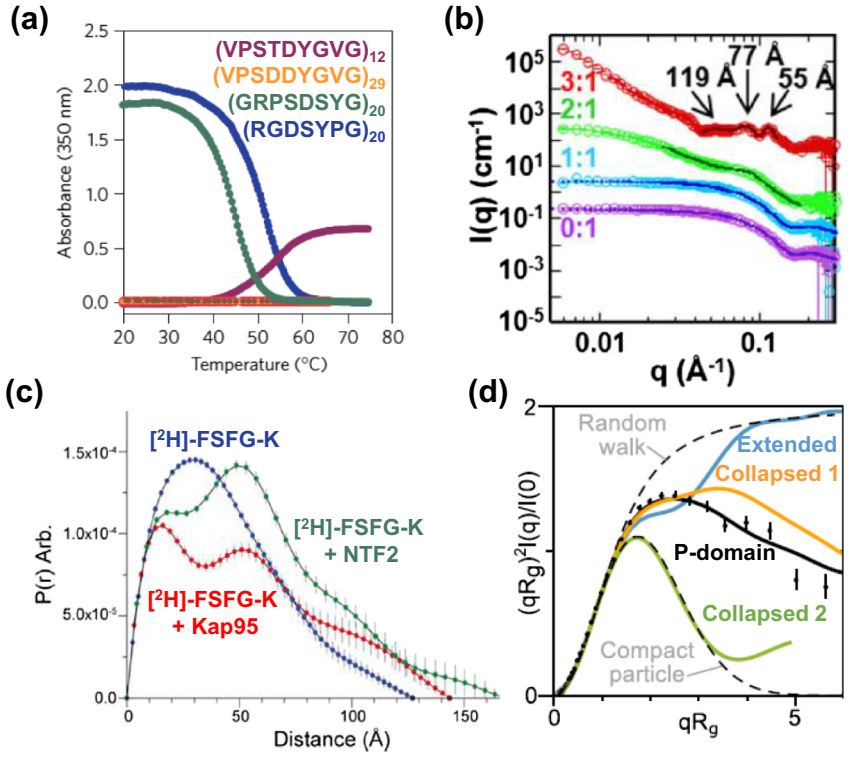

Fig. 5. Light and particle scattering methods for characterization of membrane-less bodies. (a) Turbidity curves as a function of temperature demonstrating that the U/LCST and the critical temperature for demixing of protein polymers can be tuned through changes in their amino acid composition. The figure was reproduced with permission from Quiroz and Chilkoti [156]. (b) Neutron scattering profiles of NPM1 N-terminal domain titrated with rpL5 peptide at the indicated rpL5:NPM1 molar ratios, across the phase boundary. The red curve illustrates the demixed state and reveals correlation distances that correspond to regular spacing between NPM1 molecules that are cross-linked by the rpL5 peptide. This figure was reproduced from Mitrea *et al.* [138]. (c) Pairwise distance distribution analysis of SANS curves for FSFG-K nucleoporin in the absence (blue) and presence of the transport factors Kap95 (red) and NTF2 (green). FGFG-K is isotopically labeled with ^{2}H, while the transport factors were prepared with natural isotopic abundance; data were collected under buffer conditions that match the neutron scattering of the latter, and thus represent the contribution of FSFG-K in the two-component system, illustrating differential conformational changes in the FSFG-K chain conformation upon interaction with transport factors. The figure was reproduced with permission from Sparks *et al.* [161]. (d) Dimension-less Kratky analysis of SAXS scattering for the P-domain of Pab1 (black), along with the back-calculated curves for computationally derived conformers [extended (blue), collapsed on itself (orange) and collapsed on the purification His-tag (green)], and theoretical profiles for a fully random walk and compact particle (dashed lines). The figure was reproduced with permission from Riback *et al.* [155].

mechanisms by which precursor protein clusters form [169].

Given the intrinsically low particle length scale resolution of light scattering methods, a change of 3-fold or larger in mass and/or radius is often required for reliable, quantitative interpretation of structural rearrangements and/or complexation [165, 166]. Solutions used in these measurements should be homogenous and free of any particulate matter, and thus, it is advisable that they are filtered or centrifuged prior to use. Individual components should be measured alongside mixtures, as controls, to ensure sample monodispersity; large aggregates will cause artefactual scattering. Caution is required in the quantitative interpretation of molecular size (mass and hydrodynamic radius) derived from DLS measurements, as this information is obtained from the diffusion coefficient, which is interpreted using an assumed molecular shape model. Particularly, for proteins with heterogeneous shapes (i.e., a mix of folded domains and disordered regions), the assumed shape models can lead to inaccurate conclusions. The size of demixed core micelles formed between a cationic linear polymer and anionically supercharged proteins was quantitatively resolved using DLS [170]. In this case, DLS-based quantification of particle size was informative, because the formed particles were spherical in shape and uniform in size.

Small-angle scattering

Small-angle scattering (SAS) analysis is well suited for the low-resolution (1–2 nm) determination of molecular size and shape and can provide useful insights into the mechanisms of biomolecular interactions and conformational transitions with respect to stoichiometry and arrangement. SAS studies are most applicable for particles with sizes ranging from

5 kDa to 100 MDa (1 nm–1 μm) and can provide useful structural information in the form of molecular envelopes [154, 171–173]. In SAS experiments, isotropic scattering at low angles of either X-rays (scattered by electrons) or neutrons (scattered through interactions with nuclear spin and potential) of a polymer solution is radially averaged to calculate a scattering curve represented as the scattering intensity, $I(q)$, *versus* the scattering angle, (q) (Fig. 5b; reviewed in refs. [154, 171–173]). SAS is inherently a contrast method where signal arises from the differences between the scattering length density of solute particles and the solvent, from either the electron or nuclear spin density for X-rays and neutrons, respectively [154, 171–173]. SAS methods can be applied to many material states (liquid solutions, gels, fibers, gases, etc.); here we focus on liquid solutions and gels.

The radius of gyration (R_g), which describes the overall size of the biomolecule, can be accurately determined from SAS experiments, using several mathematical analyses. Using the Guinier approximation, R_g can be determined from the linear fit of the scattering intensity at very low scattering angles ($q < \sim 1/R_g$), (Eq. (13)),

$$I(s) = I(0)\ \exp\left(-\frac{q^2 {R_g}^2}{3}\right) \qquad (13)$$

where q is the scattering angle and $I(0)$ is the forward scattering, which is proportional to the molecular weight and concentration of the biomolecule. Fourier transformation of the scattering curve into real space yields the pairwise distance distribution function, $P(r)$ (Eq. (14)),

$$P(r) = \frac{r^2}{2\pi^2}\int_0^\infty \frac{q^2 I(q)\ \sin(qr)}{qr}\, dq \qquad (14)$$

where r is the interatomic distance. The $P(r)$ plot thus represents a histogram of all possible interatomic distances within the volume of the particle (Fig. 5c) and is used to extract size and shape information, including the maximum dimension (D_{max}) and the volume of the particle. The R_g can also be calculated from the $P(r)$ function using Eq. (15),

$$R_g^2 = \frac{\int_0^{D_{max}} r^2 P(r) dr}{2\int_0^{D_{max}} P(r) dr} \qquad (15)$$

which often provides more accurate results compared to the Guinier approximation, particularly for disordered systems. In addition, the Kratky plot ($q^2 I$ (q) *versus* q) provides a semi-quantitative approach for estimating the compaction states of proteins or polymers, where scattering curves for compact particles (e.g., globular proteins) exhibit a characteristic bell shape, partially disordered proteins (e.g., globular proteins with disordered domains) plateau at high scattering angles, and completely disordered proteins exhibit an initial plateau followed by a monotonic increase in scattering intensity (Fig. 5d). The use of dimensionless Kratky plots, which are normalized by R_g, allows for the comparison of scattering from macromolecules of different masses or conformational states. User-friendly analysis software packages, such as ATSAS [174], SasView (www.sasview.org), and ScÅtter (http://www.bioisis.net/tutorial/9) are freely available and provide comprehensive tools for extracting structural data.

Small-angle X-ray scattering

Small-angle X-ray scattering (SAXS) is particularly useful for characterization of conformational changes within, and binding events between, biomolecules in monodisperse solutions [173, 175–177]. The resolving power is superior to that of DLS, enabling detection of changes in polymer compaction state (Fig. 5c, d) [27, 155]. SAXS has been used to illustrate the importance of chain compaction of the stress granule protein Pab1 driven by hydrophobic contacts to induce phase separation [155]. Formation of higher-order complexes between multivalent Src homology domain (SH3) fusion protein and its multivalent proline-rich motif (PRM) ligand, prior to phase separation and within the light phase, was illustrated using SAXS [9].

Accurate interpretation of SAXS data requires that the particles being analyzed are monodisperse in solution. Aggregation, the presence of oligomers, and conformational heterogeneity in the sample convolute the scattering profile, rendering interpretation difficult. Several algorithms, including SASSIE [178] and EOM [175, 179], compute scattering curves using weighted analysis of the contribution of mixes species. Since SAXS scattering curves represent an underdetermined problem, caution should be exercised in the interpretation of these computational results. Size-exclusion chromatography (SEC) is often combined with SAXS (SEC-SAXS) [155, 180] to eliminate aggregates from the samples immediately prior to data collection. SEC-SAXS provides means to eliminate aggregates that form during sample shipping to SAXS beamlines at remote synchrotrons. Particular care should be taken to match the buffer for accurate subtraction of its contribution from the total scattering signal. Unlike DLS, prolonged exposure to high-intensity X-ray radiation is potentially destructive to the sample. The radiation damaging effect can be minimized through the use of flow cells [181].

Data are often collected at high flux X-ray beam lines located at synchrotrons. Here, complementary ultra-small-angle and/or wide-angle X-ray scattering approaches can expand the length scale for which structural data can be obtained to <1- to ~1000-nm length scale regimes, with smaller angles allowing for the observation of larger particles and wide angles for the measurement of finer structural details [182–184]. An additional advantage for SAXS data collection is the ability to use bench-top instruments with in-house X-ray sources. However, the lower X-ray flux produced by bench-top instruments requires longer exposure times.

Small-angle neutron scattering

In contrast to X-ray scattering, neutron scattering intensity, or scattering length, is dependent on the number of neutrons and can thus be modulated by different isotopes. Of particular importance is the fact that the scattering lengths of protons (^{1}H) and deuterons (^{2}H) exhibit opposite signs, a property that can be exploited to selectively observe one component within multicomponent assemblies. The scattering length densities of protonated proteins and nucleic acids are intrinsically different, and therefore, adjusting the D_2O/H_2O ratio of the solvent to match one or the other component allows for detection of the scattering contribution of the unmatched component only, in the context of the complex [185]. Because proteins exhibit similar scattering length densities, selective contrast matching is often not possible. In such cases, one of the proteins within the complex is isotopically labeled with deuterium (e.g., expressed in bacteria grown in minimal media containing 70% ^2H_2O, to attain ~50% incorporation of ^{2}H at non-exchangeable positions) to increase its buffer matching $^2H_2O/^1H_2O$ ratio compared to that of, for example, a protonated protein binding partner. Scattering curves of each individual binding partner as part of the complex, combined with the full scattering curve of the protonated complex, provide additional details regarding the orientation of each individual component [185]. Contrast-matching small-angle neutron scattering (SANS) was applied to demonstrate that the FG-rich repeat disordered domain of a nucleoporin expands upon interaction with transcription factors (Fig. 5c) [161], opposite to other systems where collapse is often observed [161]. DLS was used in conjunction with SANS to confirm the absence of aggregation in the sample. The conformational ensemble was determined using the EOM [175] analysis software package [161]. SANS was also used to characterize the size and the "fuzzy spheres" shape of complex coacervated core micelles of supercharged proteins and cationic polymers [170].

Given the fact that SANS is a specialized technique that can only be applied at neutron sources (~20 in the world), it is often coupled with the higher contrast, more accessible SAXS, to provide complementary information [186, 187]. A major advantage of collecting neutron scattering data at a specialized neutron source facility is the versatility of environments and sample preparation formats that can be utilized. Characterization of organic polymers using neutron scattering, as well as mathematical models for determining the correlation distances that characterize inter-chain spacing within gel-like polymeric demixed solutions, is well established and therefore easily translatable to studies of proteins that undergo phase separation in biology. For example, correlation distances measured with SANS in heterotypic phase-separated bodies formed between NPM1 and rpL5 demonstrated that their liquid-like matrix is formed by NPM1 pentamers connected *via* the rpL5 peptides [138].

The structure analysis methods discussed above yield parameters that are ensemble averaged (NMR) or reflect all conformations present in the ensemble (scattering methods), and also require samples containing large numbers of molecules. In contrast, single-molecule detection techniques allow for detailed analyses of the conformations of individual biomolecules prior to and after phase separation. Furthermore, computational methods enable collections of individual molecules to be analyzed, providing the opportunity to understand the intermolecular interactions that drive phase separation. These two types of methods are discussed next.

Single-Molecule Fluorescence Spectroscopy

Direct observation of diffusional and conformational dynamics of macromolecules during the process of demixing and within phase-separated bodies presents several challenges, primarily related to heterogeneity of molecular size and conformational state, and conformational exchange [14]. The high sensitivity of fluorescence detectors allows for data collection from individual molecules within ensembles, enabling the scope of conformational heterogeneity to be directly examined on the sub-nm- to ~100-nm length scale [188–190]. In single-molecule fluorescence spectroscopy, the macromolecule of interest is chemically [14, 15, 27] or genetically [191] coupled to a fluorescent probe, such as a small chemical dye or a fluorescent protein, respectively. Site-specific labeling of proteins is commonly done using fluorescent dyes with thiol-reactive moieties, which covalently bind to cysteine residues [192]. Site-directed mutagenesis is employed to replace native cysteine residues and introduce new ones at specific positions, to probe structure and dynamics, while minimally affecting protein conformation [15, 27, 192]. Amine-reactive dyes are also used [14], when precise positioning of the fluorophore is not critical. A confocal fluorescence microscope equipped with high-sensitivity photon counting detectors is used to record fluorescence fluctuations within a small

volume (femtoliter) of a solution containing a labeled protein at a low concentration (pico- to nanomolar). To date, single-molecule fluorescence has received only limited application in studies of membrane-less organelles. Below, we review the application of Förster-resonance energy transfer (FRET) and fluorescence correlation-based applications to study conformational changes associated with macromolecular demixing [15, 25, 27], and to analyze the compositional features of membrane-less bodies *in vitro* [14] and in live cells [191].

Single-molecule FRET

FRET is commonly used to study inter- and intramolecular interactions, as well as conformational changes within macromolecules [189, 193, 194]. A donor and an acceptor fluorescent probe (i.e., protein or chemical dye), genetically or covalently attached to different interacting molecules or to different positions within the same macromolecule, are used as reporters of proximity between the labeled positions by measuring the ratio between the donor and acceptor fluorescence emission upon donor excitation [194]. The energy transfer efficiency (E_{FRET}, Eq. (16)) is proportional to the distance between the two fluorophores (R) and the Förster radius (R_0), and can be calculated from the emission intensity of the donor (I_D) and acceptor (I_A) (Eq. (17)) [188, 189]. Alternatively, E_{FRET} can be calculated from the change in fluorescence lifetime (Eq. (18)) of the donor only (τ_D) and the donor in the presence of acceptor (τ_{DA}) [188, 189].

$$E_{FRET} = \frac{1}{1 + \left(\frac{R}{R_0}\right)^6} \tag{16}$$

$$E_{FRET}(t) \approx \frac{I_A(t)}{I_A(t) + I_D(t)} \tag{17}$$

$$E_{FRET} = 1 - \frac{\tau_{DA}}{\tau_D} \tag{18}$$

By labeling the extremities of a single-stranded RNA molecule with a Cy3/Cy5 FRET pair and measuring FRET efficiency at the single-molecule level (smFRET), Elbaum-Garfinkle *et al.* [25] demonstrated that as the system approached the phase boundary, the interacting LAF-1-RNA molecules exhibited distinct dynamic features in the mixed *versus* demixed phase, with increased molecular fluctuations observed under conditions favoring phase separation. smFRET was also applied to study the conformational rearrangements that accompany phase separation of NPM1 (Fig. 6a) [27, 138]. In Mitrea *et al.* [27], NPM1 was labeled with the AlexaFluor488/AlexaFluor594 FRET pair at specific sites within the IDR and C-terminal folded domain and demonstrated by smFRET analysis that ionic strengths that disfavor phase separation cause conformational expansion of the disordered domain, while populating a broad conformational landscape [27]. In addition, through a similar approach, the acidic tract A2 within the IDR was shown to undergo a conformational change, extending away from the folded pentameric core, upon phase separation [138]. In these studies, a low concentration of fluorescently labeled protein (nanomolar) was introduced into a higher concentration of unlabeled molecules (micromolar) to enable fluorescence detection of single molecules. When measurements are performed in the dense phase of a phase-separated system, the fraction of fluorescently labeled molecules needs to be adjusted according to the partitioning coefficient. As discussed in the Solution turbidity section, light scattering of the droplets in the form of absorbance at wavelengths >320 nm is interpreted as turbidity and leveraged as a measurement of phase separation. The same light scattering can be a source of artifacts in fluorescence-based experiments. In order to minimize these artifacts, selection of FRET fluorescent dye pairs in the red and far-red spectral region is recommended, where turbidity effects are negligible [138]. Due to slow diffusion of demixed NPM1 molecules into, within, and out of the focal volume, the smFRET measurements within the phase-separated solution exhibit unconventional "fluorescent waves" (prolonged periods of fluorescence emission from slowly diffusing, sparsely labeled NPM1 molecules within the molecular networks that underlie phase separation) rather than the short-duration bursts of fluorescence emission associated with freely diffusing molecules or molecular assemblies [138].

Fluorescence correlation spectroscopy

Fluorescence correlation spectroscopy (FCS) enables quantitative analysis of molecular diffusion by measuring fluctuations of fluorescence intensity of labeled molecules within very small (femtoliter) focal volumes [195]. FCS is used to determine diffusion coefficients and fluorophore concentrations for labeled molecule both *in vitro* and in live cells, as well as to monitor conformational fluctuations and to probe the thermodynamics and kinetics of inter- and intra-molecular interactions [195]. For example, Maharana *et al.* [191] used FCS in cells to monitor the diffusion of FUS in the nucleus and cytoplasm. The resulting autocorrelation curves were best fit by a two-component model, suggesting that both fast- and slow-diffusing FUS molecules are present in cells. Additional FCS measurements showed that mutations that inhibited RNA binding reduced the slow-diffusing population (Fig. 6b), demonstrating that FUS is partially bound to RNA in live cells. Furthermore, the results showed an increase in the

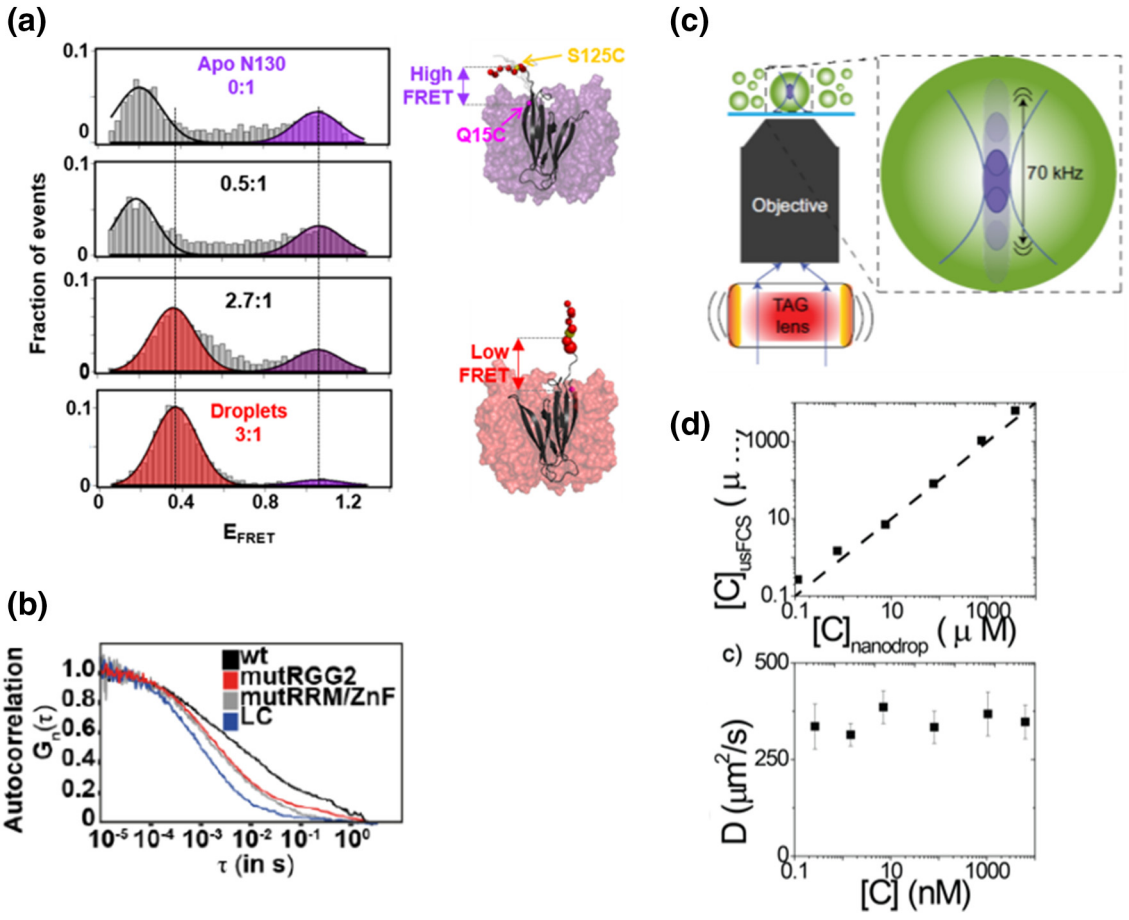

Fig. 6. Single-molecule fluorescence techniques. (a) NPM1 N-terminal domain titrations with rpL5 peptide, at the specified peptide:protein molar ratio, monitored by smFRET between two FRET probes placed on the folded domain and the disordered tail, across the phase boundary, show a decrease in FRET efficiency, indicative of an extension of the disordered tail away from the folded core. The figure was reproduced from Mitrea *et al.* [138]. (b) FCS curves of FUS-GFP constructs [wild-type protein (black), LC domain (blue) and RNA-binding deficient mutants (red and gray)] measured in the nuclei of live cells; disruption of RNA binding causes an increase in the fast-diffusing FUS-GFP population. The figure was reproduced with permission from Maharana *et al.* [191]. (c) Schematic representation of the optical set-up for ufFCS and (d) the usFCS-derived measurements of concentration (top) and diffusion (bottom) of 14-nm fluorescent polystyrene bead in solution. Panels c and d were reproduced with permission from Wei *et al.* [14].

RNA-bound FUS population in the nucleus *versus* cytoplasm, supporting the hypothesis that RNA binding modulates the phase behavior of prion-like proteins such as FUS [191].

Several technical limitations need to be considered when applying FCS for characterization of membrane-less organelles and *in vitro* phase-separated bodies. These include differences in the refractive indexes of the light and dense phases, which can lead to artifacts in the quantification of the focal volume, and convoluted effects of viscosity, molecular weight heterogeneity, and the effects of quinary interaction on the measured diffusion coefficients. Modifications of the FCS configuration, such as 2-focus FCS [196] and Z-scan ultra-fast scanning FCS (usFCS; Fig. 6c) [197], utilize internal calibration, therefore eliminating artifacts associated with determination of the size and geometry of the focal volume based on an external reference. For example, usFCS was applied to determine protein concentrations and diffusivity within the light and dense phases of a LAF-1 phase-separated system (Fig. 6c, d), allowing for quantitation of both arms of the binodal curve [14].

The examples above demonstrate that single-molecule fluorescence techniques are powerful tools for studying the structural and dynamic features of proteins within phase-separated bodies; however, the current publications have only begun to tap the full potential of these techniques. We anticipate that single-molecule fluorescence methods will experience increased use in the future to expand our molecular understanding of membrane-less organelles and other phase-separated structures *in vitro* and in cells.

In summary, the methods discussed above address broad ranges of length and timescales relevant to the structural and dynamic features of proteins and nucleic acids within membrane-less organelles. However, due to technical limitations, it is not possible to directly observe collections of individual molecules across the entirety of these length and timescales, so to understand, for example, how intermolecular networks form and drive the process of phase separation. Computational methods can bridge these gaps in experimental knowledge, as discussed below.

Computational Methods

A survey of the primary sequence and predicted secondary structures of a protein can provide important initial insights into its propensity for phase separation. Several predictors are user-friendly and freely available. The propensity for structural disorder can be accurately predicted by IUPred (http://iupred.enzim.hu/) [198, 199]. Hydrophobicity, charge distribution, and compaction state of IDRs can be predicted using CIDER (pappulab.wustl.edu/CIDER/analysis/) [200], and structural features and functional annotations of proteins or transcripts can be predicted using the SuperFamily Database [201]. The DisMeta server (http://www-nmr.cabm.rutgers.edu/bioinformatics/disorder/) [202] provides a concise report of multiple prediction results, including secondary structure, trans-membrane helices, various motifs, sequence complexity, and disorder using several algorithms. While none of these algorithms predict whether a protein is prone to phase separation *per se*, they are useful in identifying features commonly associated with phase separation based on experimental studies (e.g., short linear motifs, charge/hydrophobicity distribution, etc.).

The bioinformatics methods discussed above can be used in proteome wide searches to identify other proteins with properties associated with phase separation [13, 23, 37, 138, 150]. When coupled with analysis of gene ontology (GO) terms [203, 204], correlations between amino-acid composition, physicochemical properties of proteins, sub-cellular localization, and function can be established. For example, by computationally threading the human proteome through structures of short linear motifs that mediate gelation of LC domains, Hughes *et al*. [150] identified 2500 proteins that contain similar LC, aromatic-rich, kinked segments (LARKS), many of which are found associated with membrane-less organelles. Furthermore, a bioinformatics analysis of the proteome of stress granules by Dellaire *et al*. [18] showed an enrichment in RNA-binding, ATP-dependent helicases, and protein remodeling enzymes. This provided new insights into the, still unclear, biological function of stress granules [18]. In addition, Forman-Kay and colleagues discussed the prevalence of π–π interactions in proteins capable of undergoing phase separation and developed a predictor of phase separation propensity based on this property [205].

Concomitant with the rapid progress in the field of chemical polymers, a little over half a century ago, theoretical models that describe and predict the solubility and compaction of polymeric chains also flourished. Flory–Huggins theory [6] mathematically describes the configurational entropy of mixing of a polymer (Eq. (19)), using a simplified lattice model, taking into account polymer valency, represented as the number of lattice sites occupied by the polymer (N_1) and the solvent (N_2), and the temperature- (T-) dependent interaction strength between polymer chains (χ):

$$\frac{\Delta F_{\text{mix}}}{k_B T} = \frac{\varnothing}{N_1} \ln\varnothing + \frac{(1-\varnothing)}{N_2} \ln(1-\varnothing) + \chi\varnothing(1-\varnothing) \quad (19)$$

where Φ represents the volume fraction occupied by the polymer.

Based on fundamental chemical similarities between proteins and organic polymers, this simplified model was used to predict the phase behavior of a two-component, heterotypic system of polySH3: polyPRM, as a function of protein valency [9], and to fit experimentally determined coexistence curves for the homotypic Ddx4 system [10]. The physical basis for the layered architecture of nucleoli was also determined through an *in silico* strategy that employed Flory–Huggins theory in combination with coarse grained modeling of a tripartite system comprised of NPM1, FIB1, and a model rRNA (Fig. 7) [15]. Features parameterized during modeling that could reproduce experimental observations included the topology of the polymer (linear or branched), solvation state of the polymer modules, interaction valency (number of modules), and a matrix of pairwise interaction coefficients (between polymer modules). The resulting model attributes the preference for the FIB1-dense phase to be engulfed by the NPM1-dense phase to a higher interaction strength (χ) within the former phase, compared to the latter, which correlates with the respective surface tension values of the two phases in contact with the solvent [15]. A similar approach was used for *in silico* reconstitution of the internal organization and partitioning of RNA and proteins in nuclear speckles in five or six component, heterogeneous systems [11]. Course-grained methods, which are computationally efficient, require prior knowledge of the system (e.g., the identities of interacting elements, their pairwise affinities, and valency numbers), thereby limiting their *a priori* application. Although less computationally demanding compared to atomistic simulations (discussed below), these methods still require significant computational power, especially for multi-component systems.

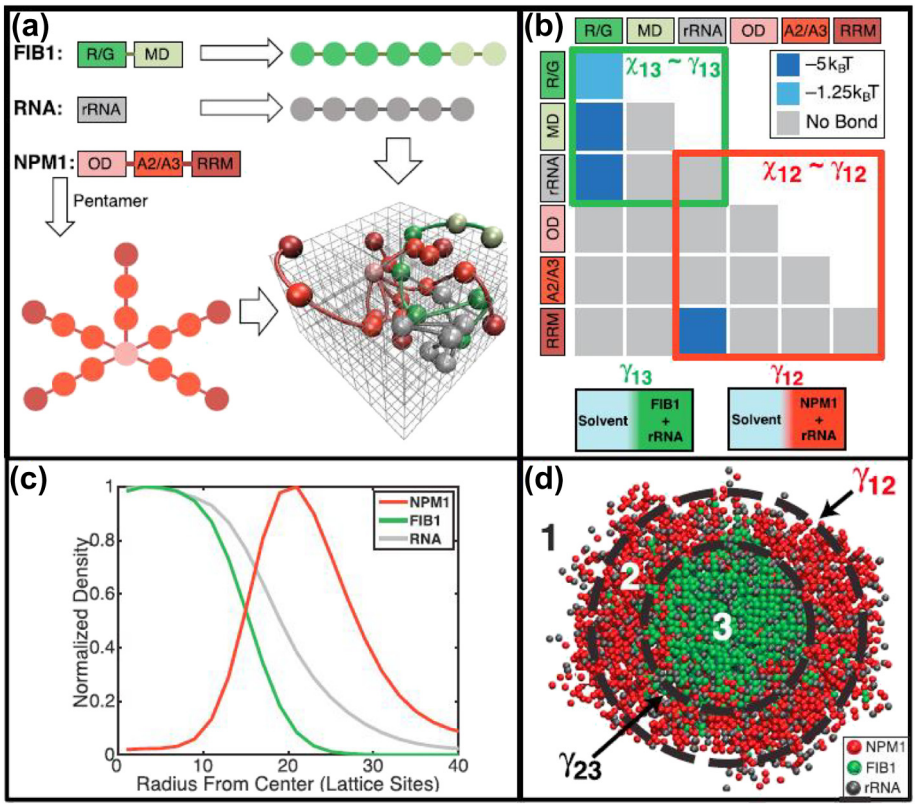

Fig. 7. Coarse-grained modeling explains nucleolar architecture. Coarse-grained modeling of a three-component system of FIB1 (abundant protein in the DFC), NPM1 (abundant protein in GC), and RNA. (a) The topology of modeled polymers. (b) Pairwise interaction matrix representing interaction energies between the modeled domains within the three polymers. (c) Distribution profiles of the three polymers within the model lattice. (d) Graphical representation of the self-organization of the three polymers based on the coarse-grained modeling results, showing an FIB1-rich core, embedded within an NPM1-rich shell, which reproduces the natural nucleolar architecture. The figure was reproduced with permission from Feric *et al.* [15].

Atomistic simulations were employed to characterize the mechanism of demixing of the intracellular domain of Nephrin; the data, which were experimentally validated, revealed a counter-ion mediated association *via* charge neutralization between the negatively charged motifs of Nephrin and the positively charged motifs on its binding partners [13]. Though informative, atomistic approaches are computationally intensive; thus, there has been a preference for coarse-grained modeling in the biological phase separation field.

Being a simplified model, Flory–Huggins theory performs well in conjunction with coarse grained modeling, but does not account for individual amino acids nor for the physicochemical differences between the 20 different amino acids (e.g., charged *versus* uncharged, polar *versus* hydrophobic, etc.). Therefore, in order to determine sequence-specific contributions to the phase behavior of a protein, more complex theories are required. Lin *et al.* [206] used an augmented Random Phase Approximation theory to account for contributions arising from sequence-specific electrostatic interactions. In this system, traditional Random Phase Approximation theory is combined with Flory–Huggins theory to accommodate charge patterning and short range interactions [206]. In order to create an *in silico* framework for studying protein phase separation, Dignon *et al.* [207] combined coarse-grained modeling with slab simulations, which simulate the light and the dense phases at equilibrium. Each amino acid was represented as a single particle, with an associated chemical potential, to calculate residue specific interactions. The method accurately reproduced experimentally derived parameters for FUS and LAF-1 (i.e., phase diagrams, critical temperatures, and saturation concentrations) and allowed for prediction of the effects of IDR chain length, valency, and folded domains on the phase boundary.

Wei *et al.* [14] reported puzzling experimental usFCS data, showing that LAF-1 partitioned within *in vitro* droplets at concentrations lower than expected. Flory–Huggins theory was unable to reproduce the two arms of the experimentally determined phase diagrams. Atomistic simulations, using the CAMPARI

software package and ABSINTH implicit solvent model, revealed large-scale conformational fluctuations within the RGG domain of LAF-1, which accounted for deviations from the simple Flory–Huggins model. Muthukumar theory, an advanced theoretical model which accounts for chain density fluctuations and two- and three-body interactions, successfully reproduced the experimental findings. In addition, this novel approach allowed for determination of the polymer network mesh size—the size cutoff past which molecular diffusion within the droplet microenvironment is hindered [14]. In addition, Harmon *et al*. [12] expanded on Flory–Huggins theory by employing the Flory–Stockmayer theory and a bead and tether model developed by Semenov and Rubinstein [208, 209], using coarse-grained and atomistic simulations, to determine the effect of the linker solvation volume on a protein's propensity to gelate with or without phase separation.

The results discussed above clearly demonstrate how computational approaches can complement experimental methods in studies of biological phase separation. Sequence analysis algorithms provide guidance on the phase separation propensity of disordered proteins and the results can be used to prioritize experimental studies when large groups of proteins are being considered. Computational modeling based on extensions of Flory–Huggins theory has provided insights into the physical mechanisms promoting phase separation and has expanded our understanding of the biology of membrane-less organelles. As computing power increases and modeling methods are improved, we anticipate that computational approaches will soon be able to explain the collective behavior of heterogeneous, phase-separated assemblies on length and timescales that approach those associated with phase-separated structures in cells.

Outlook on the Future

Multi-disciplinary efforts, many times combining concepts and methods from polymer physics, biophysics, and cell biology, and applying advanced fluorescence microscopy imaging methods, have dramatically expanded our understanding of the composition, and structural and dynamic features of membrane-less organelles. For example, we now appreciate that nucleoli are multi-layered, fluid structures whose hierarchical architecture derives from differences in the surface tensions of the different layers [15]. And we understand that these surface tension differences are associated with different affinities for rRNA and physicochemical properties of at least two key scaffolding proteins, FIB1 and NPM1, that respectively “organize” the two outer layers of the nucleolus through phase separation. Furthermore, we know that NPM1 engages in phase separation with multiple substrates *via* multiple mechanisms, and that the nature of this complex network can be modulated through changes in substrate concentration [27]. However, while scientists have amassed this wealth of knowledge through the application of many of the methods and concepts discussed herein, we understand very little about how the various types of phase separation that occur within the nucleolus mediate its function of synthesizing, processing and assembling rRNA with ribosomal proteins to build highly complex pre-ribosomal particles.

Knowledge gaps of comparable magnitude exist in association with many other membrane-less organelles, despite numerous remarkable discoveries regarding their molecular compositions, fluid properties, sub-structural features, and cellular localizations. Our molecular-level understanding of cellular processes began by relating atomic-resolution 3D structures of proteins to their molecular functions, for example, how moieties in the active site of an enzyme promote formation of transition states and chemical catalysis. More recently, we have gained knowledge of how IDPs perform diverse biological functions, for example, how some IDPs serve as signaling conduits to control kinases that gate cell division [210]. However, these examples, which relate both highly ordered protein structure and protein disorder to biological function, involve discrete molecular entities. The process of phase separation necessarily relies upon the collective behavior of many discrete molecules, causing their condensation into the micron-sized structures we call membrane-less organelles.

Fundamental questions concerning the relationship between a membrane-less organelle's structure and its function remain open (Fig. 8): How does this collective behavior, which imposes a higher level of molecular order than exists in less dense regions of the cell, promote the biological processes that occur within membrane-less organelles? How do the atomic-scale structural and dynamic features of proteins and nucleic acid molecules (i.e., DNA, RNA) drive the formation of transient molecular networks that underlie phase separation? How do the features of these networks relate to the material properties of the resulting, micron-scale fluid structures? How are complex mixtures of biomolecules, which perform particular biological processes, specifically recruited into membrane-less organelles? And how is their assembly and disassembly regulated?

The experimental methods, conceptual frameworks, and computational approaches reviewed here provide tools for addressing these and many other fundamentally important questions on the relationships between the “structure” of membrane-less organelles and their biological functions. However, there is a great need for innovation in the future to develop approaches that address the complex structural, dynamic, and organizational features, and specialized biology, associated with membrane-less

organelles. For example, rapid molecular motions, often required for maintaining the liquid-like material properties of a membrane-less organelle, which in turn modulate its function, can be quantitatively characterized using NMR spectroscopy. However, these measurements require the protein of interest to be isotopically labeled, be present at concentrations above 10 μM, and exhibit high local flexibility on the ps to ns timescale to narrow resonances. Due to these requirements, all of the studies published to date on the structure and dynamics of proteins involved in phase separation [10, 15, 16] have been limited to purified, recombinant proteins (often truncated), reconstituted in solutions containing one, or at most two, components—far from the complexity of *in vivo* systems. Single-molecule fluorescence methods have been

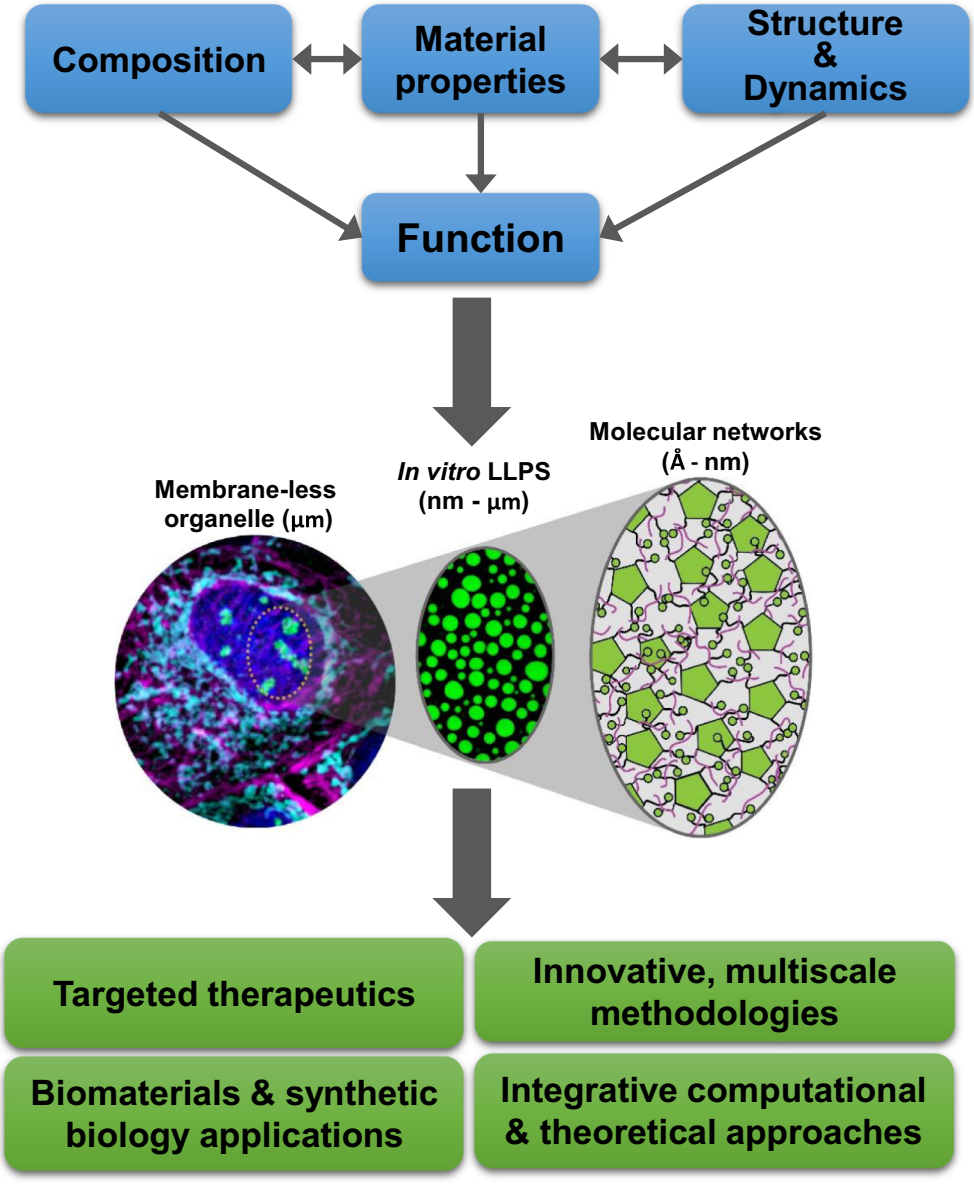

Fig. 8. Integrative approaches shed light on the structure–function relationship in membrane-less organelles and biomaterials. The function of membrane-less organelles is tightly tuned *via* the composition and the viscoelastic properties of the extended macromolecular network, and thermodynamic and kinetic properties of the intermolecular interactions between its components, which also dictate the material properties of the organelle. A thorough understanding of these relationships will build the foundation for new discoveries in the field of targeted therapeutics, biomaterials, and synthetic biology, as well as development of innovative, multi-scale methodologies, and integrative computational and theoretical approaches. The fluorescence microscopy image of a mammalian cell is courtesy of Dr. Cliff Guy.

applied to studies of *in vitro* phase-separated bodies [14, 15] and of proteins inside live cells [191, 211]. Further development and optimization of in-cell NMR methods (reviewed in ref. [212]) and single-molecule fluorescence technologies are likely to provide insights into the structure and dynamics of macromolecules within membrane-less organelles in live cells and how these properties are influenced by changes in cellular conditions.

Conceptual and computational frameworks enable prediction of how perturbations to the components of membrane-less organelles will affect their structure and function. These predictions must be accompanied in the future by tests of their validity using experimental methods that address that vast range of length and timescales pertinent to membrane-less organelles and that monitor how perturbations affect biological function, cellular behavior, and, ultimately, an organism's phenotype. A detailed understanding of the rules that govern the assembly, disassembly and reorganization of macromolecular phase-separated systems could be leveraged to design targeted therapeutics for treatment of debilitating disorders, such as neurodegenerative diseases, where the function of membrane-less organelles is disrupted, as well as to develop novel biomaterials (Fig. 8).

We hope that this review will serve as a useful guidepost for scientists in the future to discover how membrane-less organelles and other biological structures formed through phase separation enable the molecular processes that are essential for life.

Acknowledgments

This work was supported by National Institutes of Health grant 5RO1GM115634 (to R.K.), and St. Jude Children's Research Hospital and ALSAC. The authors thank Dr. Cliff Guy of the Department of Immunology for the microscopy image in Fig. 8 and the Cell and Tissue Imaging core staff for helpful discussions, both at St. Jude Children's Research Hospital.

Received 15 May 2018;
Received in revised form 4 July 2018;
Accepted 9 July 2018
Available online 24 July 2018

Keywords:
membrane-less;
organelles;
methods;
phase;

†These authors contributed equally.

‡While we have endeavored to comprehensively review the current literature, we regret that important work from many scientists could not be discussed here due to length limitations. We apologize to those whose work was not included.

Abbreviations used:
DIC, differential interference contrast; ROI, region of interest; FIB1, fibrillarin; FRAP, fluorescence recovery after photobleaching; FLIP, fluorescence loss in photobleaching; SIM, structured illumination microscopy; STORM, stochastic optical reconstruction microscopy; LLSM, lattice light-sheet microscopy; TEM, transmission electron microscopy; CLEM, correlated light and electron microscopy; FISH, fluorescence *in situ* hybridization; cryo-EM, cryo-electron microscopy; IDPs, intrinsically disordered proteins; CSP, chemical shift perturbation; IDRs, intrinsically disordered regions; NOE, nuclear Overhauser effect; PFG, pulse field gradient; ELP, elastin-like polypeptide; cryo-ET, cryo-electron tomography; FIB, focused ion beam; DLS, dynamic light scattering; SLS, static light scattering; SAS, small-angle scattering; SAXS, small-angle X-ray scattering; SEC, size-exclusion chromatography; SANS, small-angle neutron scattering; FRET, Förster-resonance energy transfer; FCS, fluorescence correlation spectroscopy; EM, electron microscopy.

References

[1] G.E. Palade, Structure and function at the cellular level, JAMA 198 (8) (1966) 815–825.
[2] G. Pianese, Beitrag zur histologie und aetiologie der carcinoma. histologische und experimentelle untersuchungen, Beitr. Pathol. Anat. Allg. Pathol. 142 (1896) 1–193.
[3] C.P. Brangwynne, et al., Germline P granules are liquid droplets that localize by controlled dissolution/condensation, Science 324 (5935) (2009) 1729–1732.
[4] C.P. Brangwynne, T.J. Mitchison, A.A. Hyman, Active liquid-like behavior of nucleoli determines their size and shape in *Xenopus laevis* oocytes, Proc. Natl. Acad. Sci. U. S. A. 108 (11) (2011) 4334–4339.
[5] P.J. Flory, Thermodynamics of high polymer solutions, J. Chem. Phys. 10 (1) (1942) 51–61.
[6] P.J. Flory, Statistical thermodynamics of semi-flexible chain molecules, Proc. R. Soc. Lond. A 234 (1196) (1956) 60–73.
[7] M.L. Huggins, The viscosity of dilute solutions of long-chain molecules. IV. Dependence on concentration, J. Am. Chem. Soc. 64 (11) (1942) 2716–2718.
[8] J.T.G. Overbeek, M. Voorn, Phase separation in polyelectrolyte solutions. Theory of complex coacervation, J. Cell. Physiol. 49 (S1) (1957) 7–26.
[9] P. Li, et al., Phase transitions in the assembly of multivalent signalling proteins, Nature 483 (7389) (2012) 336–340.
[10] J.P. Brady, et al., Structural and hydrodynamic properties of an intrinsically disordered region of a germ cell-specific protein on phase separation, Proc. Natl. Acad. Sci. U. S. A. 114 (39) (2017) E8194–E8203.

[11] J. Fei, et al., Quantitative analysis of multilayer organization of proteins and RNA in nuclear speckles at super resolution, J. Cell Sci. 130 (24) (2017) 4180–4192.
[12] T.S. Harmon, et al., Intrinsically disordered linkers determine the interplay between phase separation and gelation in multivalent proteins, elife 6 (2017).
[13] C.W. Pak, et al., Sequence determinants of intracellular phase separation by complex coacervation of a disordered protein, Mol. Cell 63 (1) (2016) 72–85.
[14] M.T. Wei, et al., Phase behaviour of disordered proteins underlying low density and high permeability of liquid organelles, Nat. Chem. 9 (11) (2017) 1118–1125.
[15] M. Feric, et al., Coexisting liquid phases underlie nucleolar subcompartments, Cell 165 (7) (2016) 1686–1697.
[16] K.A. Burke, et al., Residue-by-residue view of in vitro FUS granules that bind the C-terminal domain of RNA polymerase II, Mol. Cell 60 (2) (2015) 231–241.
[17] D. Chen, S. Huang, Nucleolar components involved in ribosome biogenesis cycle between the nucleolus and nucleoplasm in interphase cells, J. Cell Biol. 153 (1) (2001) 169–176.
[18] G. Dellaire, et al., The number of PML nuclear bodies increases in early S phase by a fission mechanism, J. Cell Sci. 119 (Pt 6) (2006) 1026–1033.
[19] A.H. Fox, et al., Paraspeckles: a novel nuclear domain, Curr. Biol. 12 (1) (2002) 13–25.
[20] L. Fu, et al., Nuclear aggresomes form by fusion of PML-associated aggregates, Mol. Biol. Cell 16 (10) (2005) 4905–4917.
[21] S. Weidtkamp-Peters, et al., Dynamics of component exchange at PML nuclear bodies, J. Cell Sci. 121 (Pt 16) (2008) 2731–2743.
[22] M. Dundr, T. Misteli, M.O. Olson, The dynamics of postmitotic reassembly of the nucleolus, J. Cell Biol. 150 (3) (2000) 433–446.
[23] T.J. Nott, et al., Phase transition of a disordered nuage protein generates environmentally responsive membraneless organelles, Mol. Cell 57 (5) (2015) 936–947.
[24] A. Molliex, et al., Phase separation by low complexity domains promotes stress granule assembly and drives pathological fibrillization, Cell 163 (1) (2015) 123–133.
[25] S. Elbaum-Garfinkle, et al., The disordered P granule protein LAF-1 drives phase separation into droplets with tunable viscosity and dynamics, Proc. Natl. Acad. Sci. U. S. A. 112 (23) (2015) 7189–7194.
[26] S. Ambadipudi, et al., Liquid–liquid phase separation of the microtubule-binding repeats of the Alzheimer-related protein Tau, Nat. Commun. 8 (1) (2017) 275.
[27] D.M. Mitrea, et al., Self-interaction of NPM1 modulates multiple mechanisms of liquid–liquid phase separation, Nat. Commun. 9 (1) (2018) 842.
[28] H. Falahati, et al., Nucleation by rRNA dictates the precision of nucleolus assembly, Curr. Biol. 26 (3) (2016) 277–285.
[29] C.A. Combs, H. Shroff, Fluorescence microscopy: a concise guide to current imaging methods, Curr. Protoc. Neurosci. 79 (2017) 2 1 1–2 1 25.
[30] J.L. Liu, M. Buszczak, J.G. Gall, Nuclear bodies in the *Drosophila* germinal vesicle, Chromosom. Res. 14 (4) (2006) 465–475.
[31] K.H. Lee, et al., C9orf72 dipeptide repeats impair the assembly, dynamics, and function of membrane-less organelles, Cell 167 (3) (2016) 774–788 (e17).
[32] S. Jain, et al., ATPase-modulated stress granules contain a diverse proteome and substructure, Cell 164 (3) (2016) 487–498.
[33] M. Platani, et al., In vivo analysis of Cajal body movement, separation, and joining in live human cells, J. Cell Biol. 151 (7) (2000) 1561–1574.
[34] J.R. Wheeler, et al., Distinct stages in stress granule assembly and disassembly, elife 5 (2016).
[35] H. Falahati, E. Wieschaus, Independent active and thermodynamic processes govern the nucleolus assembly in vivo, Proc. Natl. Acad. Sci. U. S. A. 114 (6) (2017) 1335–1340.
[36] A.R. Strom, et al., Phase separation drives heterochromatin domain formation, Nature 547 (7662) (2017) 241–245.
[37] T.M. Franzmann, et al., Phase separation of a yeast prion protein promotes cellular fitness, Science 359 (6371) (2018).
[38] C. Molenaar, K.L. Weeks, Nucleocytoplasmic shuttling: the ins and outs of quantitative imaging, Clin. Exp. Pharmacol. Physiol. (2018).
[39] D.B. Murphy, M.W. Davisdson, Fundamentals of Light Microscopy and Electronic Imaging, John Wiley & Sons, Hoboken, NJ, 2012.
[40] V. Centonze Frohlich, Phase contrast and differential interference contrast (DIC) microscopy, J. Vis. Exp. 17 (2008).
[41] J.L. Liu, et al., The *Drosophila* melanogaster Cajal body, J. Cell Biol. 172 (6) (2006) 875–884.
[42] D.M. Chudakov, et al., Fluorescent proteins and their applications in imaging living cells and tissues, Physiol. Rev. 90 (3) (2010) 1103–1163.
[43] I. Nikic, et al., Labeling proteins on live mammalian cells using click chemistry, Nat. Protoc. 10 (5) (2015) 780–791.
[44] H.C. Ishikawa-Ankerhold, R. Ankerhold, G.P. Drummen, Advanced fluorescence microscopy techniques—*FRAP, FLIP, FLAP, FRET and FLIM*, Molecules 17 (4) (2012) 4047–4132.
[45] T. Suzuki, et al., Recent advances in fluorescent labeling techniques for fluorescence microscopy, Acta Histochem. Cytochem. 40 (5) (2007) 131–137.
[46] M. Rashidian, J.K. Dozier, M.D. Distefano, Enzymatic labeling of proteins: techniques and approaches, Bioconjug. Chem. 24 (8) (2013) 1277–1294.
[47] V. Liss, et al., Self-labelling enzymes as universal tags for fluorescence microscopy, super-resolution microscopy and electron microscopy, Sci. Rep. 5 (2015) 17740.
[48] A.S. Boutorine, et al., Fluorescent probes for nucleic acid visualization in fixed and live cells, Molecules 18 (12) (2013) 15357–15397.
[49] M. Biancalana, S. Koide, Molecular mechanism of thioflavin-T binding to amyloid fibrils, Biochim. Biophys. Acta 1804 (7) (2010) 1405–1412.
[50] T. Nomura, et al., Intranuclear aggregation of mutant FUS/TLS as a molecular pathomechanism of amyotrophic lateral sclerosis, J. Biol. Chem. 289 (2) (2014) 1192–1202.
[51] V.I. Stsiapura, et al., Thioflavin T as a molecular rotor: fluorescent properties of thioflavin T in solvents with different viscosity, J. Phys. Chem. B 112 (49) (2008) 15893–15902.
[52] J. Jonkman, C.M. Brown, Any way you slice it-a comparison of confocal microscopy techniques, J. Biomol. Tech. 26 (2) (2015) 54–65.
[53] Y. Garini, I.T. Young, G. McNamara, Spectral imaging: principles and applications, Cytometry A 69 (8) (2006) 735–747.

[54] S.C. Weber, C.P. Brangwynne, Inverse size scaling of the nucleolus by a concentration-dependent phase transition, Curr. Biol. 25 (5) (2015) 641–646.
[55] S.F. Banani, et al., Compositional control of phase-separated cellular bodies, Cell 166 (3) (2016) 651–663.
[56] C. Fink, F. Morgan, L.M. Loew, Intracellular fluorescent probe concentrations by confocal microscopy, Biophys. J. 75 (4) (1998) 1648–1658.
[57] A. Jain, R.D. Vale, RNA phase transitions in repeat expansion disorders, Nature 546 (7657) (2017) 243–247.
[58] J.R. Lakowicz (Ed.), Principles of Fluorescence Spectroscopy, 3rd ed.Springer, Boston, MA, 2006.
[59] T.J. Nott, T.D. Craggs, A.J. Baldwin, Membraneless organelles can melt nucleic acid duplexes and act as biomolecular filters, Nat. Chem. 8 (6) (2016) 569–575.
[60] S.T. Hess, et al., Quantitative analysis of the fluorescence properties of intrinsically fluorescent proteins in living cells, Biophys. J. 85 (4) (2003) 2566–2580.
[61] R.M. Martin, et al., Principles of protein targeting to the nucleolus, Nucleus 6 (4) (2015) 314–325.
[62] J.T. Mika, et al., Measuring the viscosity of the *Escherichia coli* plasma membrane using molecular rotors, Biophys. J. 111 (7) (2016) 1528–1540.
[63] M.A. Haidekker, et al., New fluorescent probes for the measurement of cell membrane viscosity, Chem. Biol. 8 (2) (2001) 123–131.
[64] N. Loren, et al., Fluorescence recovery after photobleaching in material and life sciences: putting theory into practice, Q. Rev. Biophys. 48 (3) (2015) 323–387.
[65] J. Braga, J.M. Desterro, M. Carmo-Fonseca, Intracellular macromolecular mobility measured by fluorescence recovery after photobleaching with confocal laser scanning microscopes, Mol. Biol. Cell 15 (10) (2004) 4749–4760.
[66] A. Patel, et al., A liquid-to-solid phase transition of the ALS protein FUS accelerated by disease mutation, Cell 162 (5) (2015) 1066–1077.
[67] C.A. Day, et al., Analysis of protein and lipid dynamics using confocal fluorescence recovery after photobleaching (FRAP), Curr. Protoc. Cytom. 62 (2012) 2.19-1–2.19.29 (Chapter 2: p. Unit2 19).
[68] M. Kang, et al., Simplified equation to extract diffusion coefficients from confocal FRAP data, Traffic 13 (12) (2012) 1589–1600.
[69] F. Pincet, et al., FRAP to characterize molecular diffusion and interaction in various membrane environments, PLoS One 11 (7) (2016), e0158457.
[70] B.L. Sprague, et al., Analysis of binding reactions by fluorescence recovery after photobleaching, Biophys. J. 86 (6) (2004) 3473–3495.
[71] J.S. Andersen, et al., Nucleolar proteome dynamics, Nature 433 (7021) (2005) 77–83.
[72] E. Louvet, et al., Probing the stiffness of isolated nucleoli by atomic force microscopy, Histochem. Cell Biol. 141 (4) (2014) 365–381.
[73] R.A. Finch, P.K. Chan, ATP depletion affects NPM translocation and exportation of rRNA from nuclei, Biochem. Biophys. Res. Commun. 222 (2) (1996) 553–558.
[74] D.M. Mitrea, et al., Structural polymorphism in the N-terminal oligomerization domain of NPM1, Proc. Natl. Acad. Sci. U. S. A. 111 (12) (2014) 4466–4471.
[75] D. Bertwistle, M. Sugimoto, C.J. Sherr, Physical and functional interactions of the Arf tumor suppressor protein with nucleophosmin/B23, Mol. Cell. Biol. 24 (3) (2004) 985–996.
[76] A.J. Apicelli, et al., A non-tumor suppressor role for basal p19(ARF) in maintaining nucleolar structure and function, Mol. Cell. Biol. 28 (3) (2008) 1068–1080.
[77] Y. Lin, et al., Formation and maturation of phase-separated liquid droplets by RNA-binding proteins, Mol. Cell 60 (2) (2015) 208–219.
[78] V.H. Ryan, et al., Mechanistic view of hnRNPA2 low-complexity domain structure, interactions, and phase separation altered by mutation and arginine methylation, Mol. Cell 69 (3) (2018) 465–479 (e7).
[79] Z. Monahan, et al., Phosphorylation of the FUS low-complexity domain disrupts phase separation, aggregation, and toxicity, EMBO J. 36 (20) (2017) 2951–2967.
[80] D.T. Murray, et al., Structure of FUS protein fibrils and its relevance to self-assembly and phase separation of low-complexity domains, Cell 171 (3) (2017) 615–627 (e16).
[81] E.L. Guenther, et al., Atomic structures of TDP-43 LCD segments and insights into reversible or pathogenic aggregation, Nat. Struct. Mol. Biol. 25 (6) (2018) 463–471.
[82] S. Wegmann, et al., Tau protein liquid–liquid phase separation can initiate tau aggregation, EMBO J. 37 (7) (2018).
[83] D. Hernandez-Verdun, et al., The nucleolus: structure/function relationship in RNA metabolism, Wiley Interdiscip. Rev. RNA 1 (3) (2010) 415–431.
[84] A.M. Sydor, et al., Super-resolution microscopy: from single molecules to supramolecular assemblies, Trends Cell Biol. 25 (12) (2015) 730–748.
[85] J. Demmerle, et al., Strategic and practical guidelines for successful structured illumination microscopy, Nat. Protoc. 12 (5) (2017) 988–1010.
[86] F. Kraus, et al., Quantitative 3D structured illumination microscopy of nuclear structures, Nat. Protoc. 12 (5) (2017) 1011–1028.
[87] D.L. Spector, A.I. Lamond, Nuclear speckles, Cold Spring Harb. Perspect. Biol. (2011) 3(2).
[88] T. Ha, P. Tinnefeld, Photophysics of fluorescent probes for single-molecule biophysics and super-resolution imaging, Annu. Rev. Phys. Chem. 63 (2012) 595–617.
[89] G.T. Dempsey, et al., Evaluation of fluorophores for optimal performance in localization-based super-resolution imaging, Nat. Methods 8 (12) (2011) 1027–1036.
[90] B. Huang, M. Bates, X. Zhuang, Super-resolution fluorescence microscopy, Annu. Rev. Biochem. 78 (2009) 993–1016.
[91] B.C. Chen, et al., Lattice light-sheet microscopy: imaging molecules to embryos at high spatiotemporal resolution, Science 346 (6208) (2014) 1257998.
[92] J.T. Wang, et al., Regulation of RNA granule dynamics by phosphorylation of serine-rich, intrinsically disordered proteins in *C. elegans*, elife 3 (2014), e04591.
[93] E.V. Orlova, H.R. Saibil, Structural analysis of macromolecular assemblies by electron microscopy, Chem. Rev. 111 (12) (2011) 7710–7748.
[94] U. Scheer, D. Weisenberger, The nucleolus, Curr. Opin. Cell Biol. 6 (3) (1994) 354–359.
[95] V. Sirri, D. Hernandez-Verdun, P. Roussel, Cyclin-dependent kinases govern formation and maintenance of the nucleolus, J. Cell Biol. 156 (6) (2002) 969–981.
[96] J.G. Gall, et al., Assembly of the nuclear transcription and processing machinery: Cajal bodies (coiled bodies) and transcriptosomes, Mol. Biol. Cell 10 (12) (1999) 4385–4402.
[97] O. Bounedjah, et al., Free mRNA in excess upon polysome dissociation is a scaffold for protein multimerization to form stress granules, Nucleic Acids Res. 42 (13) (2014) 8678–8691.

[98] S. Souquere, et al., Unravelling the ultrastructure of stress granules and associated P-bodies in human cells, J. Cell Sci. 122 (Pt 20) (2009) 3619–3626.
[99] M. Kato, et al., Cell-free formation of RNA granules: low complexity sequence domains form dynamic fibers within hydrogels, Cell 149 (4) (2012) 753–767.
[100] Y. Lin, et al., Toxic PR poly-dipeptides encoded by the C9orf72 repeat expansion target LC domain polymers, Cell 167 (3) (2016) 789–802 (e12).
[101] A.M. Janke, et al., Lysines in the RNA polymerase II C-terminal domain contribute to TAF15 fibril recruitment, Biochemistry 57 (17) (2017) 2549–2563.
[102] S. Souquere, D. Weil, G. Pierron, Comparative ultrastructure of CRM1-nucleolar bodies (CNoBs), Intranucleolar bodies (INBs) and hybrid PML/p62 bodies uncovers new facets of nuclear body dynamic and diversity, Nucleus 6 (4) (2015) 326–338.
[103] D.P. Bazett-Jones, M.J. Hendzel, Electron spectroscopic imaging of chromatin, Methods 17 (2) (1999) 188–200.
[104] P. de Boer, J.P. Hoogenboom, B.N. Giepmans, Correlated light and electron microscopy: ultrastructure lights up! Nat. Methods 12 (6) (2015) 503–513.
[105] C. Normand, et al., Correlative light and electron microscopy of nucleolar transcription in *Saccharomyces cerevisiae*, Methods Mol. Biol. 1455 (2016) 29–40.
[106] P. Tchelidze, et al., Nucleolar sub-compartments in motion during rRNA synthesis inhibition: contraction of nucleolar condensed chromatin and gathering of fibrillar centers are concomitant, PLoS One 12 (11) (2017), e0187977.
[107] E. Smirnov, et al., Reproduction of the FC/DFC units in nucleoli, Nucleus 7 (2) (2016) 203–215.
[108] D. Oberti, et al., Dicer and Hsp104 function in a negative feedback loop to confer robustness to environmental stress, Cell Rep. 10 (1) (2015) 47–61.
[109] A. Soranno, et al., Single-molecule spectroscopy reveals polymer effects of disordered proteins in crowded environments, Proc. Natl. Acad. Sci. U. S. A. 111 (13) (2014) 4874–4879.
[110] A.S. Holehouse, R.V. Pappu, Collapse transitions of proteins and the interplay among backbone, sidechain, and solvent interactions, Annu. Rev. Biophys. (2018).
[111] D. Weihs, T.G. Mason, M.A. Teitell, Bio-microrheology: a frontier in microrheology, Biophys. J. 91 (11) (2006) 4296–4305.
[112] M. Feric, C.P. Brangwynne, A nuclear F-actin scaffold stabilizes ribonucleoprotein droplets against gravity in large cells, Nat. Cell Biol. 15 (10) (2013) 1253–1259.
[113] T.P. Kole, Y. Tseng, D. Wirtz, Intracellular microrheology as a tool for the measurement of the local mechanical properties of live cells, Methods Cell Biol. 78 (2004) 45–64.
[114] H. Zhang, et al., RNA controls polyQ protein phase transitions, Mol. Cell 60 (2) (2015) 220–230.
[115] A. Hernandez-Vega, et al., Local nucleation of microtubule bundles through tubulin concentration into a condensed Tau phase, Cell Rep. 20 (10) (2017) 2304–2312.
[116] J.G. McNally, et al., Three-dimensional imaging by deconvolution microscopy, Methods 19 (3) (1999) 373–385.
[117] A.E. Conicella, et al., ALS mutations disrupt phase separation mediated by alpha-helical structure in the TDP-43 low-complexity C-terminal domain, Structure 24 (9) (2016) 1537–1549.
[118] M.P. van de Corput, F.G. Grosveld, Fluorescence in situ hybridization analysis of transcript dynamics in cells, Methods 25 (1) (2001) 111–118.
[119] R.W. Dirks, et al., Synthesis, processing, and transport of RNA within the three-dimensional context of the cell nucleus, Crit. Rev. Eukaryot. Gene Expr. 9 (3–4) (1999).
[120] S. Kwon, Single-molecule fluorescence in situ hybridization: quantitative imaging of single RNA molecules, BMB Rep. 46 (2) (2013) 65.
[121] P.C. Havugimana, et al., A census of human soluble protein complexes, Cell 150 (5) (2012) 1068–1081.
[122] E.L. Huttlin, et al., Architecture of the human interactome defines protein communities and disease networks, Nature 545 (7655) (2017) 505–509.
[123] E.L. Huttlin, et al., The BioPlex network: a systematic exploration of the human interactome, Cell 162 (2) (2015) 425–440.
[124] J.S. Andersen, et al., Directed proteomic analysis of the human nucleolus, Curr. Biol. 12 (1) (2002) 1–11.
[125] Y. Ahmad, et al., NOPdb: nucleolar proteome database—2008 update, Nucleic Acids Res. 37 (Database issue) (2009) D181–D184.
[126] M. Rosner, K. Schipany, M. Hengstschlager, Merging high-quality biochemical fractionation with a refined flow cytometry approach to monitor nucleocytoplasmic protein expression throughout the unperturbed mammalian cell cycle, Nat. Protoc. 8 (3) (2013) 602–626.
[127] S. Boulon, et al., The nucleolus under stress, Mol. Cell 40 (2) (2010) 216–227.
[128] J.Y. Youn, et al., High-density proximity mapping reveals the subcellular organization of mRNA-associated granules and bodies, Mol. Cell 69 (3) (2018) 517 (–+).
[129] D.I. Kim, et al., Probing nuclear pore complex architecture with proximity-dependent biotinylation, Proc. Natl. Acad. Sci. 111 (24) (2014) E2453–E2461.
[130] B.D. Freibaum, J.P. Taylor, The role of dipeptide repeats in C9ORF72-related ALS-FTD, Front. Mol. Neurosci. 10 (2017) 35.
[131] D.M. Mitrea, R.W. Kriwacki, Phase separation in biology; functional organization of a higher order, Cell Commun. Signal 14 (1) (2016) 1.
[132] A. Khong, et al., The stress granule transcriptome reveals principles of mRNA accumulation in stress granules, Mol. Cell 68 (4) (2017) 808–820 (e5).
[133] S. Namkoong, et al., Systematic characterization of stress-induced RNA granulation, Mol. Cell 70 (1) (2018) 175–187 (e8).
[134] K.C. Hadley, et al., Determining composition of micron-scale protein deposits in neurodegenerative disease by spatially targeted optical microproteomics, elife 4 (2015).
[135] A. Hubstenberger, et al., P-body purification reveals the condensation of repressed mRNA regulons, Mol. Cell 68 (1) (2017) 144–157 (e5).
[136] E.B. Gibbs, E.C. Cook, S.A. Showalter, Application of NMR to studies of intrinsically disordered proteins, Arch. Biochem. Biophys. 628 (2017) 57–70.
[137] J. Cavanagh, et al., Protein NMR Spectroscopy, Academic Press, 2006.
[138] D.M. Mitrea, et al., Nucleophosmin integrates within the nucleolus via multi-modal interactions with proteins displaying R-rich linear motifs and rRNA, elife 5 (2016).
[139] G.T. Debelouchina, T.W. Muir, A molecular engineering toolbox for the structural biologist, Q. Rev. Biophys. 50 (2017), e7.
[140] W. Bermel, et al., Exclusively heteronuclear (13) C-detected amino-acid-selective NMR experiments for the study of

intrinsically disordered proteins (IDPs), Chembiochem 13 (16) (2012) 2425–2432.
[141] S. Chhabra, et al., (15)N detection harnesses the slow relaxation property of nitrogen: delivering enhanced resolution for intrinsically disordered proteins, Proc. Natl. Acad. Sci. U. S. A. 115 (8) (2018) E1710–E1719.
[142] E.B. Gibbs, R.W. Kriwacki, Direct detection of carbon and nitrogen nuclei for high-resolution analysis of intrinsically disordered proteins using NMR spectroscopy, Methods 138-139 (2018) 39–46.
[143] S.E. Reichheld, et al., Direct observation of structure and dynamics during phase separation of an elastomeric protein, Proc. Natl. Acad. Sci. U. S. A. 114 (22) (2017) E4408–E4415.
[144] T. Yuwen, J.P. Brady, L.E. Kay, Probing conformational exchange in weakly interacting, slowly exchanging protein systems via off-resonance R1rho experiments: application to studies of protein phase separation, J. Am. Chem. Soc. 140 (6) (2018) 2115–2126.
[145] M. Renault, A. Cukkemane, M. Baldus, Solid-state NMR spectroscopy on complex biomolecules, Angew. Chem. Int. Ed. Engl. 49 (45) (2010) 8346–8357.
[146] H.R. Dannatt, et al., Weak and transient protein interactions determined by solid-state NMR, Angew. Chem. Int. Ed. Engl. 55 (23) (2016) 6638–6641.
[147] M. Kato, Y. Lin, S.L. McKnight, Cross-beta polymerization and hydrogel formation by low-complexity sequence proteins, Methods 126 (2017) 3–11.
[148] M. Sunde, et al., Common core structure of amyloid fibrils by synchrotron X-ray diffraction, J. Mol. Biol. 273 (3) (1997) 729–739.
[149] W.T. Astbury, S. Dickinson, K. Bailey, The X-ray interpretation of denaturation and the structure of the seed globulins, Biochem. J. 29 (10) (1935) 2351–2360 1.
[150] M.P. Hughes, et al., Atomic structures of low-complexity protein segments reveal kinked beta sheets that assemble networks, Science 359 (6376) (2018) 698–701.
[151] K.Y. Shi, et al., Toxic PRn poly-dipeptides encoded by the C9orf72 repeat expansion block nuclear import and export, Proc. Natl. Acad. Sci. U. S. A. 114 (7) (2017) E1111–E1117.
[152] M. Schaffer, et al., Optimized cryo-focused ion beam sample preparation aimed at in situ structural studies of membrane proteins, J. Struct. Biol. 197 (2) (2017) 73–82.
[153] F.J.B. Bauerlein, et al., In situ architecture and cellular interactions of polyQ inclusions, Cell 171 (1) (2017) 179–187 (e10).
[154] N. Zaccai, I. Serdyuk, J. Zaccai, Methods in Molecular Biophysics: Structure, Dynamics, Function for Biology and Medicine, 2 ed. Cambridge University Press, New York, NY, 2017.
[155] J.A. Riback, et al., Stress-triggered phase separation is an adaptive, evolutionarily tuned response, Cell 168 (6) (2017) 1028–1040 (e19).
[156] F.G. Quiroz, A. Chilkoti, Sequence heuristics to encode phase behaviour in intrinsically disordered protein polymers, Nat. Mater. 14 (11) (2015) 1164–1171.
[157] C.S. Cummings, A.C. Obermeyer, Phase separation behavior of supercharged proteins and polyelectrolytes, Biochemistry 57 (3) (2018) 314–323.
[158] A.S. Raut, D.S. Kalonia, Pharmaceutical perspective on opalescence and liquid–liquid phase separation in protein solutions, Mol. Pharm. 13 (5) (2016) 1431–1444.
[159] C. Ishimoto, T. Tanaka, Critical behavior of a binary mixture of protein and salt water, Phys. Rev. Lett. 39 (8) (1977) 474–477.
[160] T. Tanaka, C. Ishimoto, L.T. Chylack Jr., Phase separation of a protein–water mixture in cold cataract in the young rat lens, Science 197 (4307) (1977) 1010–1012.
[161] S. Sparks, et al., Deciphering the “fuzzy” interaction of FG nucleoporins and transport factors using small-angle neutron scattering, Structure 26 (3) (2018) 477–484.e4.
[162] H. Nishi, et al., Phase separation of an IgG1 antibody solution under a low ionic strength condition, Pharm. Res. 27 (7) (2010) 1348–1360.
[163] A.G. Larson, et al., Liquid droplet formation by HP1alpha suggests a role for phase separation in heterochromatin, Nature 547 (7662) (2017) 236–240.
[164] S. Schutz, E.R. Noldeke, R. Sprangers, A synergistic network of interactions promotes the formation of in vitro processing bodies and protects mRNA against decapping, Nucleic Acids Res. 45 (11) (2017) 6911–6922.
[165] A.P. Minton, Recent applications of light scattering measurement in the biological and biopharmaceutical sciences, Anal. Biochem. 501 (2016) 4–22.
[166] J. Stetefeld, S.A. McKenna, T.R. Patel, Dynamic light scattering: a practical guide and applications in biomedical sciences, Biophys. Rev. 8 (4) (2016) 409–427.
[167] G. Wu, et al., Elucidating the weak protein-protein interaction mechanisms behind the liquid–liquid phase separation of a mAb solution by different types of additives, Eur. J. Pharm. Biopharm. 120 (2017) 1–8.
[168] J.R. Simon, et al., Programming molecular self-assembly of intrinsically disordered proteins containing sequences of low complexity, Nat. Chem. 9 (6) (2017) 509–515.
[169] D. Soraruf, et al., Protein cluster formation in aqueous solution in the presence of multivalent metal ions—a light scattering study, Soft Matter 10 (6) (2014) 894–902.
[170] A.C. Obermeyer, et al., Complex coacervation of supercharged proteins with polyelectrolytes, Soft Matter 12 (15) (2016) 3570–3581.
[171] D.I. Svergun, Small-angle X-ray and neutron scattering as a tool for structural systems biology, Biol. Chem. 391 (7) (2010) 737–743.
[172] P. Bernado, et al., Solution scattering approaches to dynamical ordering in biomolecular systems, Biochim. Biophys. Acta 1862 (2) (2018) 253–274.
[173] B.N. Chaudhuri, Emerging applications of small angle solution scattering in structural biology, Protein Sci. 24 (3) (2015) 267–276.
[174] D. Franke, et al., ATSAS 2.8: a comprehensive data analysis suite for small-angle scattering from macromolecular solutions, J. Appl. Crystallogr. 50 (4) (2017) 1–14.
[175] P. Bernado, et al., Structural characterization of flexible proteins using small-angle X-ray scattering, J. Am. Chem. Soc. 129 (17) (2007) 5656–5664.
[176] C.E. Blanchet, D.I. Svergun, Small-angle X-ray scattering on biological macromolecules and nanocomposites in solution, Annu. Rev. Phys. Chem. 64 (2013) 37–54.
[177] A.G. Kikhney, D.I. Svergun, A practical guide to small angle X-ray scattering (SAXS) of flexible and intrinsically disordered proteins, FEBS Lett. 589 (19 Pt A) (2015) 2570–2577.
[178] J.E. Curtis, et al., SASSIE: a program to study intrinsically disordered biological molecules and macromolecular ensembles using experimental scattering restraints, Comput. Phys. Commun. 183 (2) (2012) 382–389.
[179] G. Tria, et al., Advanced ensemble modelling of flexible macromolecules using X-ray solution scattering, IUCrJ 2 (Pt 2) (2015) 207–217.

[180] A.W. Malaby, et al., Methods for analysis of size-exclusion chromatography–small-angle X-ray scattering and reconstruction of protein scattering, J. Appl. Crystallogr. 48 (Pt 4) (2015) 1102–1113.
[181] N. Kirby, et al., Improved radiation dose efficiency in solution SAXS using a sheath flow sample environment, Acta Crystallogr. D Struct. Biol. 72 (Pt 12) (2016) 1254–1266.
[182] F. Zhang, J. Ilavsky, Ultra-small-angle X-ray scattering of polymers, Polym. Rev. 50 (1) (2010) 59–90.
[183] M.A. Graewert, D.I. Svergun, Impact and progress in small and wide angle X-ray scattering (SAXS and WAXS), Curr. Opin. Struct. Biol. 23 (5) (2013) 748–754.
[184] R.N. Andrews, et al., An in situ USAXS–SAXS–WAXS study of precipitate size distribution evolution in a model Ni-based alloy, J. Appl. Crystallogr. 50 (Pt 3) (2017) 734–740.
[185] D.A. Jacques, J. Trewhella, Small-angle scattering for structural biology—expanding the frontier while avoiding the pitfalls, Protein Sci. 19 (4) (2010) 642–657.
[186] A. Schlundt, J.N. Tants, M. Sattler, Integrated structural biology to unravel molecular mechanisms of protein–RNA recognition, Methods 118-119 (2017) 119–136.
[187] T.N. Cordeiro, et al., Structural characterization of highly flexible proteins by small-angle scattering, Adv. Exp. Med. Biol. 1009 (2017) 107–129.
[188] D.K. Sasmal, et al., Single-molecule fluorescence resonance energy transfer in molecular biology, Nanoscale 8 (48) (2016) 19928–19944.
[189] T. Ha, Single-molecule fluorescence resonance energy transfer, Methods 25 (1) (2001) 78–86.
[190] P. Sengupta, J. Balaji, S. Maiti, Measuring diffusion in cell membranes by fluorescence correlation spectroscopy, Methods 27 (4) (2002) 374–387.
[191] S. Maharana, et al., RNA buffers the phase separation behavior of prion-like RNA binding proteins, Science 360 (6391) (2018) 918–921.
[192] P.R. Banerjee, A.A. Deniz, Shedding light on protein folding landscapes by single-molecule fluorescence, Chem. Soc. Rev. 43 (4) (2014) 1172–1188.
[193] H.P. Lu, Probing single-molecule protein conformational dynamics, Acc. Chem. Res. 38 (7) (2005) 557–565.
[194] R. Roy, S. Hohng, T. Ha, A practical guide to single-molecule FRET, Nat. Methods 5 (6) (2008) 507–516.
[195] E.L. Elson, Fluorescence correlation spectroscopy: past, present, future, Biophys. J. 101 (12) (2011) 2855–2870.
[196] T. Dertinger, et al., Two-focus fluorescence correlation spectroscopy: a new tool for accurate and absolute diffusion measurements, ChemPhysChem 8 (3) (2007) 433–443.
[197] J. Ries, P. Schwille, New concepts for fluorescence correlation spectroscopy on membranes, Phys. Chem. Chem. Phys. 10 (24) (2008) 3487–3497.
[198] Z. Dosztanyi, et al., The pairwise energy content estimated from amino acid composition discriminates between folded and intrinsically unstructured proteins, J. Mol. Biol. 347 (4) (2005) 827–839.
[199] Z. Dosztanyi, et al., IUPred: web server for the prediction of intrinsically unstructured regions of proteins based on estimated energy content, Bioinformatics 21 (16) (2005) 3433–3434.
[200] R.K. Das, R.V. Pappu, Conformations of intrinsically disordered proteins are influenced by linear sequence distributions of oppositely charged residues, Proc. Natl. Acad. Sci. U. S. A. 110 (33) (2013) 13392–13397.
[201] J. Gough, et al., Assignment of homology to genome sequences using a library of hidden Markov models that represent all proteins of known structure, J. Mol. Biol. 313 (4) (2001) 903–919.
[202] Y.J. Huang, T.B. Acton, G.T. Montelione, DisMeta: a meta server for construct design and optimization, Methods Mol. Biol. 1091 (2014) 3–16.
[203] C. The Gene Ontology, Expansion of the Gene Ontology knowledgebase and resources, Nucleic Acids Res. 45 (D1) (2017) D331–D338.
[204] M. Ashburner, et al., Gene Ontology: tool for the unification of biology. The Gene Ontology Consortium, Nat. Genet. 25 (1) (2000) 25–29.
[205] R.M. Vernon, et al., Pi–pi contacts are an overlooked protein feature relevant to phase separation, elife 7 (2018).
[206] Y.H. Lin, J.D. Forman-Kay, H.S. Chan, Sequence-specific polyampholyte phase separation in membraneless organelles, Phys. Rev. Lett. 117 (17) (2016).
[207] G.L. Dignon, et al., Sequence determinants of protein phase behavior from a coarse-grained model, PLoS Comput. Biol. 14 (1) (2018), e1005941.
[208] M. Rubinstein, A.N. Semenov, Thermoreversible gelation in solutions of associating polymers. 2. Linear dynamics, Macromolecules 31 (4) (1998) 1386–1397.
[209] A.N. Semenov, M. Rubinstein, Thermoreversible gelation in solutions of associative polymers. 1. Statics, Macromolecules 31 (4) (1998) 1373–1385.
[210] C.A. Galea, et al., Regulation of cell division by intrinsically unstructured proteins: intrinsic flexibility, modularity, and signaling conduits, Biochemistry 47 (29) (2008) 7598–7609.
[211] I. Konig, et al., Single-molecule spectroscopy of protein conformational dynamics in live eukaryotic cells, Nat. Methods 12 (8) (2015) 773–779.
[212] E. Luchinat, L. Banci, In-cell NMR: a topical review, IUCrJ 4 (Pt 2) (2017) 108–118.